Modeling of plasma-activated ammonia synthesis☆

Katja Vodlan [a,b], Blaž Likozar [a,b,c,d], Matej Huš [a,e,f,*] ⓘD

[a] Department of Catalysis and Chemical Reaction Engineering, National Institute of Chemistry, Hajdrihova 19, SI-1001 Ljubljana, Slovenia
[b] Faculty of Chemistry and Chemical Technology, University of Ljubljana, Večna pot 113, SI-1000 Ljubljana, Slovenia
[c] University of Nova Gorica, Vipavska 13, SI-5000 Nova Gorica, Slovenia
[d] Pulp and Paper Institute, Bogišićeva 8, SI-1000 Ljubljana, Slovenia
[e] Association of Technical Culture of Slovenia, Zaloška 65, SI-1000 Ljubljana, Slovenia
[f] Institute of Protection of Cultural Heritage of Slovenia, Poljanska 40, SI-1000 Ljubljana, Slovenia

ABSTRACT

In addition to its main use in agriculture as the main feedstock for fertilizer production, ammonia is investigated as a prospective energy vector in several sectors. This, however, presupposes an environmentally friendly synthesis alternative to the Haber-Bosch process. Plasma-catalytic systems seem to be the perfect candidate, as they are well suited to utilize intermittent renewable energy sources and for small-scale on-site production. Despite extensive research, plasma-catalytic systems still face challenges, particularly the low energy yield, which falls short of the Haber-Bosch process. Most research used to be based on trial-and-error testing of different catalysts and reaction conditions, but recent efforts have focused on uncovering the underlying mechanisms through various computational methods. In this review, the development of 0D plasma kinetic models is highlighted, and other modeling approaches across different scales, crucial for further advances in system efficiency and catalyst design, are analyzed.

1. Introduction

Ammonia is one of the most widely produced chemicals on the industrial scale [1] due to its irreplaceable role in fertilizer production that sustains the world's population [2]. Most of the 183 Mt of annual ammonia is still produced using conventional Haber-Bosch process, almost exclusively from natural gas, oil, and coal[3]. Although the nitrogen for ammonia production is obtained from the air, a steam-methane reforming process, which produces carbon dioxide, must be used to obtain hydrogen. Consequently, Haber-Bosch process is classified as one of the largest emitters of greenhouse gasses, accounting for 1–2 % of annual carbon dioxide emissions.[4,5] Even though ammonia synthesis is an exothermic reaction, the reaction temperature must be elevated to 600–700 K, even in the presence of a catalyst, to cleave a strong triple bond in the nitrogen molecules. In addition, the pressure must be increased to shift the equilibrium in favor of ammonia formation.[6–8] These requirements, along with the condensation of the product, results in a vast energy consumption, making the Haber-Bosch process one of the largest global energy consumers, consuming about 2 % of the global energy [5,7,9]. With the increasing demand from the food industry as a result of the ever-growing world population and emergence of new niches for ammonia, these figures could increase even further in the future. In recent years, ammonia has gained interest as a potential hydrogen carrier [10,11], as a reducing agent in post-treatment techniques for NOx emissions from combustion processes [12,13] and as a potential carbon-free fuel[13,14]. Therefore, it is of great importance to develop an alternative environmentally friendly process that would allow NH₃ synthesis under milder conditions, use of water for the hydrogen feedstock as carbon–neutral alternative to steam-methane reforming, and the implementation of cost-effective renewable electricity [15–17]. Since the Haber-Bosch process is only profitable on a large scale, ammonia production is highly centralized. In order to reduce the costs and additional carbon dioxide emissions caused by exporting the product, it is crucial that the alternative synthesis process is also suitable for local production on a smaller scale. The plasma-catalytic synthesis route has been intensively researched as an alternative to Haber-Bosch process, as it provides clean, carbon-free ammonia generation even at ambient conditions.[18–20] Plasma systems are also

---

☆ This article is part of a special issue entitled: 'ISCRE 28' published in Chemical Engineering Journal.
* Corresponding author at: Department of Catalysis and Chemical Reaction Engineering, National Institute of Chemistry, Hajdrihova 19, SI-1001 Ljubljana, Slovenia.
 E-mail address: matej.hus@ki.si (M. Huš).

ideally suited to the use of renewable energy sources due to their short response times and offer great potential for small-scale on-site ammonia production as well.[21–23] Despite the many advantages of plasma-catalytic systems, their energy yields are not yet comparable to those of the Haber-Bosch process. The maximum energy yield achieved so far with the laboratory plasma system is 35.7 g NH_3/kWh[24] while the target value for commercial use is between 150 and 200 g NH_3/kWh [25]. As shown in Table 1, most of the tested plasma-catalytic systems do not surpass the energy yield value of 5 g NH_3/kWh. The reasons for such low energy yields are low concentrations of produced ammonia, poisoning of the catalyst with hydrogen, high energy consumption of the reactor systems and ammonia splitting by plasma. [21,26].

The main challenge in optimizing such systems and developing an ideal catalyst lies in the lack of understanding of plasma-catalyst synergy and the lack of knowledge of the underlying mechanism, which is a consequence of the difficulties with *in-situ* characterization in plasma [21,27]. Catalyst screening and reactor system optimization methods have been mainly based on experimental work. However, in the last 10 years many research groups attempted to decipher the mechanism using various computational methods. For low-pressure N_2-H_2 systems with high-energy electrons and ion kinetics, a self-consistent kinetic model was proposed in the 1990 s by Gordiets *et al.*[28] based on previous findings that already considered detailed vibrational kinetics and surface reaction [29]. As plasma reaction systems operating at higher pressures are preferred for plasma catalytic synthesis of ammonia due to higher production rates and better energy efficiency, recent research has mostly been contributed to their development. In 2017, Hong *et al.* [29] made the first attempt at detailed kinetic modeling of nonequilibrium N_2–H_2 discharges at atmospheric pressure for catalytic ammonia production. After that, many efforts have been made to understand the plasma-catalytic ammonia production by multiscale modeling[30] from atomic scale using density functional theory (DFT) [17,31–33] to the mesoscale using 0D kinetic modeling [34–43], microkinetic modeling [2,8,44] and even reactor scale using computational fluid dynamics (CFD) [31]. Since plasma chemistry alone is very complex, not to mention the implementation of the synergy between plasma and catalyst, surface reactions, and plasma reactor geometries in the model, it is difficult to provide a detailed description of the reaction mechanism and the role of individual active species [44,45]. Researchers still do not agree on the rate-limiting step or the predominant reaction mechanism. Therefore, the rational determination of optimal catalyst remains a challenge.[19] .

Plasma-catalytic ammonia production has been the subject of numerous published review articles[7,15,21,27,45–52], but very few of them focused on the advances in computational modeling and simulations of such systems. As computationally led catalyst design represents an important step towards advancement of the understanding and improvement of the system's efficiency, the aim of this paper is to compare different modeling approaches used to describe the plasma-catalytic systems and compare the findings from computational simulations to experimental findings. Because the mesoscale is the most suitable for plasma modeling and has been the most intensively researched, the review focuses mainly on kinetic modeling.

2. Multiscale modeling: advantages and limitations

Advances in computational chemistry and chemical engineering have established multiscale modeling as an important tool for the design and optimization of catalytic systems, driven by the integration of multiple scales of modeling, ranging from the atomistic to the reactor scale[89].

2.1. Atomistic scale

Modeling at the atomistic scale utilizes first-principles methods to study electron interactions fundamental to catalytic processes. Due to its

favourable trade-off between computational cost and accuracy, DFT is commonly used in heterogenous catalysts. These calculations provide a detailed mechanistic insights into reaction pathways, surface interactions, and the nature of active sites, thus enabling the prediction of the catalytic activity.[30,90] However, quantum simulations alone are only relevant at 0 K. To extend the relevance of the results to higher temperatures, enthalpic and entropic contributions have to be considered, which consist of vibrational, rotational and translational contributions. These are then used in the transition state theory (TST) to obtain kinetic parameters.[91] Since TST requires identification of the transition states, which is a computationally demanding task, approximate tools are often applied, such as the Brønsted-Evans-Polanyi (BEP) relations. It states that there is a linear correlation between the activation barrier (transition state energy) and the easier-to-compute reaction energy of an elementary reaction step[92,93]. It should be noted that BEP relations are not universal but only transferrable between analogous systems.

As a ground-level method, DFT is poorly suited to describe plasma systems. Nevertheless, due to its ubiquity and lack of higher level tools, it is mostly employed for the determination of different parameters used in kinetic and microkinetic models including adsorption energies of reactive species[44], reaction energy barriers[33,44], surface reaction rate coefficients[94] and sticking coefficients[95]. DFT in this context serves as a tool to supply input parameters for higher-level kinetic models, which are usually further refined with experimental data. This approach is required due to the complexity of plasma-catalytic systems arising from the interactions between the catalyst and plasma that importantly influence the reaction dynamics. Conventional DFT used for thermal catalytic reactions does not account for the influence of electric field and fails to accurately predict the catalytic activity under plasma conditions.

Mehta *et al.*[44] demonstrated that vibrational excitations of nitrogen molecules in plasma change the linear BEP correlation, causing the shift of the volcano compared to the thermal catalytic reaction. Recent advances have, however, sought to incorporate the influence of the electric field in DFT simulations. Chen *et al.*[96] studied the effects of electric field and surface electrons on the adsorption and dissociation of nitrogen molecules on Ni and different Ru surfaces. Their DFT simulations revealed that electric field induces a redistribution of local electrons on the catalyst surface, which was determined to be the main factor in promoting nitrogen dissociation and adsorption. Their study also revealed a change in the optimal Ru active site from step sites (such as B5), typically favoured in thermal catalytic process, to terrace sites under the influence of the electric field. Shao *et al.*[97] integrated DFT in a microkinetic model while considering the change in the electric field. To model different electric fields, the Effective Screening Medium (ESM) method was employed. It enables the consideration of the influence of adsorbate on the electric field strength. While these developments mark an important milestone in plasma-catalytic multiscale model design, a time-dependent characteristic of plasma call for further improvements. Since plasma properties are highly sensitive to external factors, including the catalyst itself, the discharge cannot be treated as constant [98]. Addressing this limitation requires more computationally intensive methods, such as time-dependent DFT[97].

Another challenge arises from the complexity of the plasma-catalytic ammonia synthesis mechanism. In plasma, a diverse array of reactive species is formed, including radicals, atoms, ions, molecules as well as vibrationally and electronically excited species. Incorporating additional plasma effects and reaction parameters into kinetic models increases computational cost substantially. Given recent progress in other catalytic fields[99–103], a coupling of DFT with machine learning (ML) could provide a promising strategy to overcome these challenges by enabling more efficient catalyst screening and reaction pathway predictions.

In MD simulations, the time evolution of the system is determined by numerically integrating Newton's law of motion. Empirical classical

Table 1
Comparison of the state-of-the-art performance in the DBD plasma-catalytic ammonia production.

catalyst	H_2/N_2	Φ [mLmin^{-1}]	U [kV]	f [kHz]	T [K]	P_d [W]	e.y. [gNH$_3$kWh^{-1}]	R_{NH3} [mmolh^{-1} gcat^{-1}]	Ref
PZT	1	12	3	0.5	323	–	0.90	–	[53]
Cs-Ru (10 wt%)/CNT [a]	3	4000	6	10	299	–	2.20	–	[54]
Cs-Ru(10 wt%)/ MCM-41 [a]							1.20	–	
Cs-Ru(10 wt%)/AC [a]							0.80	–	
Ru(1 wt%)/Al$_2$O$_3$	0.67 + 0.14 H$_2$O	1000	14	13	298	–	0.70	–	[12]
Ru(2 wt%)-Mg (5 wt%)/γ-Al$_2$O$_3$ [b]	4	2000	–	–	573	7	35.70	0.80	[24]
Ni(4.5 wt%)/silica + BaTiO$_3$ [c]	air	–	20	20	523	75	4.60	–	[55]
wool-like Ag	0.33	100	5	50	–	–	–	1.99	[10]
wool-like Cu								1.63	
wool- like Pd								1.20	
wool-like Pt								1.07	
wool-like Ni								0.95	
wool-like Au								3.98	
Ru(5 wt%)/MCM-41	1	–	–	–	–	–	0.65	–	[56]
Cs(3 wt%),K(2 wt%), Ba(2 wt%)-Ru (5 wt%)/MCM-41							0.90	–	
Ni(20 wt%)/SiO$_2$	0.33	25	–	20	293	140	0.44	–	[57]
BaTiO$_3$						93	0.43	–	
Ni(20 wt%)/ SiO$_2$ + BaTiO$_3$ [d]						115	0.57	–	
Al$_2$O$_3$	0.5	210	–	9.2	513	26	1.31	0.06	[58]
Co(5 wt%)/γ-Al$_2$O$_3$	2	20	–	20	438	10	1.70	10.00	[44]
Ru(5 wt%)/γ-Al$_2$O$_3$	0.33	50	–	20–25	498	10	–	3.60	[59]
Ni(5 wt%)/γ-Al$_2$O$_3$							–	3.40	
Co(5 wt%)/γ-Al$_2$O$_3$							–	3.30	
Fe(5 wt%)/γ-Al$_2$O$_3$	0.33	55	5.1	20	473	15	–	4.62	[60]
Ni(5 wt%)/γ-Al$_2$O$_3$							–	4.80	
Co(5 wt%)/γ-Al$_2$O$_3$							–	5.22	
K(10 wt%)-Ru (2 wt%)/γ-Al$_2$O$_3$	0.25	4000	–	–	573	12	–	0.40	[61]
Cs(5 wt%)-Ru (2 wt%)/γ-Al$_2$O$_3$					603		–	0.18	
Mg(5 wt%)-Ru(2 wt%)/γ-Al$_2$O$_3$		2000			573		–	0.37	
Fe(5 wt%)/γ-Al$_2$O$_3$	0.5	40	24	9.2	308	55	0.25	0.40	[62]
Ni(5 wt%)/γ-Al$_2$O$_3$						55	0.29	0.47	
Cu(5 wt%)/γ-Al$_2$O$_3$						55	0.28	0.46	
[e] –	1	4000	6.44	23	–	–	20.50	3.24 mmol/h	[63]
SiO$_2$	3	27	17	20	298	11	0.40	–	[35]
Zeolite 5A	1	25	–	25	393	20	15.50	–	[9]
γ-Al$_2$O$_3$/acidic	3	100	–	–	363——378	24	5.75	–	[64]
γ-Al$_2$O$_3$/neutral							6.25	–	
γ-Al$_2$O$_3$/alkaline							6.58	–	
γ-Al$_2$O$_3$	3	400	40	21	713	46.7	1.05	–	[2]
α-Al$_2$O$_3$							1.01	–	
MgO							0.94	–	
CaO							0.9	–	
Ru(5 wt%)/α-Al$_2$O$_3$	0.5	120	9	20	391	38.4	1.88	–	[65]
Ru(5 wt%)/AC	3	100	–	10.1	–	21	0.72	–	[66]
Zeolite 5A	2	25	30	25	367	12	0.25	1.44	[67]
Zeolite beta						9	0.27	1.44	
L-MgO [f]	0.5	300	–	9.2	473	60	–	3.90	[68]
H-MgO [g]							–	3.30	
Al$_2$O$_3$							–	3.80	
Ru(5 wt%)/Al$_2$O$_3$							1.04	4.10	
Ru(5 wt%)/L-MgO							1.29	4.40	
Fe(5 wt%)/γ-Al$_2$O$_3$	0.5 + 0.38He	22.5 (20 He)	0.42	18.3	598	1	–	1.08	[41]
Ni(5 wt%)/γ-Al$_2$O$_3$							–	1.14	
Ni(10 wt%)/MCM-41	3	40	7.8	9.2	308	40	1.50	5.60	[26]
ZIF-8	0.67 + 1 Ar	25	–	–	367	15.5	–	2.10	[69]
ZIF-67						17.8	–	2.50	
Ni(10 wt%)/ Zeolite 13X	3	10,000	–	–	485	66	0.20	–	[70]
ZnCo(SA)–N$_2$- ZIF-67/SiO$_2$	1.5	25	14–18	8.5	423	7	0.55	2.24	[71]
K(6 wt%)-Ru (2 wt%)/MgO	1	20	10	25	663	3.8	1.23	–	[72]
TiO$_2$	1	100	6	50	296	–	–	0.60 [h]	[73]
Ni(5 wt%)/TiO$_2$							–	0.83 [h]	
Ni(5 wt%)/Al$_2$O$_3$							–	2.22 [h]	

Table 1 (*continued*)

catalyst	H_2/N_2	Φ [mL min⁻¹]	U [kV]	f [kHz]	T [K]	P_d [W]	e.y. [gNH₃kWh⁻¹]	R_{NH_3} [mmol h⁻¹ gcat⁻¹]	Ref
Fe(5 wt%)/Al₂O₃							–	0.55 [h]	
Ru(5 wt%)/Al₂O₃							–	0.18 [h]	
Al₂O₃							–	1.38 [h]	
SBA-15	3	25	8.8	25	424	1	25.10	5.30	
	3	25	8.8	25	424	1	4.60	4.10	[19]
ZIF-8	3	25	8.8	25	424	1	1.90	1.70	
Fumed SiO₂	3	25	8.8	25	424	1	1.40	1.20	
SAPO-34	3	25	8.8	25	424	1	1.20	1.10	
Non-porous SiO₂	3	25	8.8	25	424	1	1.10	1.00	
MgTiO₃	1	25	12.5	25	444	20	5.70	7.30	[74]
BaTiO₃							4.00	5.40	
SrTiO₃							2.50	4.20	
CaTiO₃							4.50	3.50	
MgTiO₃	1 + 2 He						3.70	13.70	
Zeolite 4A	1	10	10	25	330	6.4	2.30	0.42	[25]
Ni(5 wt%, 3.5 nm)/SiO₂	1	50	13.75	25	428	10.68	4.20	2.70	[1]
Ni(5 wt%, 5.6 nm)/SiO₂							8.00	6.60	
Fe(10 wt%)/γ-Al₂O₃	1	100	–	23.5	<393	67	0.51	0.17	[75]
Co(10 wt%)/γ-Al₂O₃							0.68	0.21	
Cu(10 wt%)/γ-Al₂O₃							0.57	0.19	
Ru(10 wt%)/γ-Al₂O₃							0.61	0.18	
Fe	1	25	12	25	398	15	0.16	0.03	[32]
Ni							0.19	0.04	
Cu							0.22	0.04	
Co							0.23	0.05	
Pd							0.26	0.04	
Ag							0.30	0.05	
Ru(1 wt%)/AC	1	100	13.4	10.1	373–383	9	0.65	–	[76]
Ru(1 wt%)/ZSM-5							0.52	–	
Ru(1 wt%)/α-Al₂O₃							0.40	–	
Ru(1 wt%)/SiO₂							0.34	–	
Co-Ni(5 wt%)/Al₂O₃	1	200	–	40	473	20	1.28	0.48	[77]
Ni(5 wt%)-Mg₀,₀₂/SBA-15	1	20	7.5	8	296	9	1.05	4.42	[78]
Ru(1 wt%)/MgTiO₃	1	20	12	8	–	10	1.50	2.51	[79]
Co(1 wt%)/MgTiO₃							1.45	2.38	
Ru(0.5 wt%)Co(0.5 wt%)/MgTiO₃							1.54	2.51	
Cu(5 wt%)/SiO₂	CH_4/N_2 = 2	10	–	57	310	7.36	0.25	0.34	[80]
Ru(5 wt%)/MgO	wet N₂	1000	8.23	1–40	303	4	0.07	2.67	[17]
γ-Al₂O₃	wet N₂	200	10	9	296	38	0.01	0.004	[81]
Co(3 wt%)/SiO₂	wet N₂ [i]	6.2	4.12	–	394	2	3.20	3.70	[82]
Co(10 wt%)La(10 wt%)/Al₂O₃	1	100	–	23.5	< 394	51	–	0.15	[83]
Ru(3 wt%)Ni(3 wt%)/BaTiO₃	1	–	–	9.4–9.8	296	10	0.39	–	[84]
Ni(15 wt%)/LaOF	3	25	5–10	7.9	296	13	2.70	2.10	[85,86]
Ru(2 wt%)/CeO₂	3	90	13	5	673	15.7	1.50	6.80	[86]
Ru(2 wt%)/MgO						15.2	1.30	5.80	
SAPO-11	1	25	12.1	–	365	20	–	2.88	[87]
SAPO-34								2.52	
SAPO-56								1.86	
Co-Ni(5 wt%)/Al₂O₃	1	200	40	40	473	48	0.19	0.69	[88]
Co-Ni(5 wt%)/MCM-41							0.60	2.20	
Co-Ni(5 wt%)/MOF-74							0.72	2.60	

[a] sorbent molecular sieve 13X.

[b] pulse power supply.

[c] sorbent polyHIPE.

[d] volume ratio of 1: 1.

[e] sorbent MgCl₂ and pulse density modulation of plasma.

[f] light magnesium oxide with the bulk density of 0.2 gcm⁻³ and slightly soluble in water and ethanol.

[g] heavy magnesium oxide with the bulk density of 0.5 gcm⁻³ and insoluble in water or ethanol.

[h] an average value (3.25 g) was taken into account as a catalyst's mass because the exact mass of individual catalyst was not included in the article.

[i] wet with sea water.

potentials are often used to describe molecular forces, which stem from the electrostatic and van der Waals interactions in complex systems. On the other hand, classical MD cannot account for bond breaking and formation, which are essential when describing chemical reactions. A hybrid approach with reactive force fields (ReaxFF) is required to do this but it is highly dependent on the system at hand and requires extensive parametrisation with DFT input if the force field has not been developed before.

Alternatively, ab initio molecular dynamics (AIMD) can be used, where all interactions are computed from first principles (such as DFT). This comes at a very high computational cost, especially for the systems involving a large number of electrons.[91,104] Very recently Lu et al. [105] investigated the influence of electric field on plasma-catalytic ammonia production using ReaxFF MD method. The use of this approach provided a new insight in reaction pathway in plasma-catalytic ammonia production as a new ammonia formation pathway through the hydrogenation of N_2 molecule had been identified. However, despite its advantages, this method cannot consider the effect of free electrons in plasma on enhancement of ammonia formation.

2.2. Mesoscopic scale

Mesoscale modelling requires kinetic parameters, which can be obtained from very different source. In first-principles based simulations, quantum calculations are used to generate the kinetic parameters. In more phenomenological simulations, they can be obtained from fitting the reaction mechanism to experimental data or similar. In heterogenous catalysis, kinetic Monte Carlo (kMC) and mean-field microkinetic modeling are widely used to determine rate-limiting steps and the dominating reaction pathways, both of which are critical for the catalyst development.

Additionally, surface coverage phenomena play a key role in understanding catalyst performance and deactivation in both thermal and plasma catalysis. While kMC is a stochastic method that captures spatio-temporal events, a deterministic microkinetic modeling solves a system of differential equations describing the abundance of species. kMC can provide a more detailed representation of the system and considers spatial effects, since it can account for pair-wise interactions. However, microkinetic modeling is often preferred as it is less computationally demanding.[30,90,91,106] Since this method is popular in plasma modeling, particular examples are described in the subsequent sections.

2.3. Macroscopic scale

At the macroscopic scale, reactor properties such as pressure drops and reactor geometry are simulated under operating conditions using CFD (computational fluid dynamics), which is based on the Navier-Stokes equations used to describe the motion of viscous fluids[91]. However, for industrial-scale reactor systems, the complexity of reactor geometry or the size of the reaction network might surpass the limitations of CFD. At the plan level, process simulation software like ASPEN is often used.[107].

In the field of plasma-catalysis, reactor-scale modeling is used to study the influence of the packing material on plasma behaviour. Due to the high computational demands of full 3D modeling for packed-bed DBD reactors, Van Laer et al.[108] developed two complementary axisymmetric 2D fluid models. The combination of a "contact point" model and "channel of voids" model enabled the consideration of a local electric field enhancement near the bead contact points and plasma propagation through interconnected voids. Simulations revealed that higher dielectric constants promote the formation of localized filamentary discharges between the beads, which can importantly influence the catalytic reaction.[94] With the increasing use of porous catalysts, another important aspect of fluid modeling is the study of plasma behaviour within the pores. Zhang et al.[109] designed a 2D fluid model for the simulation in a helium DBD reactor, which was later used to

study the influence of dielectric properties of packed material and the shape of the pores[94,110,111].

Coupling the aforementioned methods in an overarching model yields a multiscale model, which remains elusive. The development of such a model on all three scales would allow for a consistent description of the reaction and significantly contribute to the understanding and improving the efficiency of the plasma-catalytic systems. However, in order to achieve this, further research is required.

3. 0D plasma kinetic and microkinetic modeling

Due to the complexity and computational cost, plasma-catalytic systems are often modeled in 0D, which refers to the simplification of the models, where spatial variations in plasma physics and chemistry are ignored. Plasma-catalytic models are developed within ZDPlasKin module[112], which simulates the temporal evolution of concentrations/number densities of species in a batch reactor. The software solves the continuous equation for different species with Eq. 1[8,34,37,113]:

$$\frac{dn_i}{dt} = \sum_r c_{i,r} \bullet k_r \prod_s n_s^{c_{sr}} \tag{1}$$

where n_i is the number density of species i, $c_{i,r}$ is the stochiometric number of species i in reaction r, k_r is the rate coefficient of reaction r, n_s is the number density of reactants s and c_{sr} is the stoichiometric coefficient of reactants s in reaction r. The reaction coefficients of electron impact reactions are either determined using the electron impact cross sections as a function of electron energy and the electron energy distribution function, obtained with the Boltzmann equation solver BOLSIG+ [114] for non-Maxwellian electron energy distribution functions[43], or computed as a function of electron temperature. Similarly, reaction coefficients for gas-phase reactions of neutral species and neutralization reactions are calculated as a function of gas temperature, while ion-neutral reactions are expressed as a function of effective ion temperature [34].

Since plasma systems consist of flow, rather than batch reactors, the kinetic models had to be modified to some extent. Chen et al. [113] and Mehta et al.[38] treated the reactor system as a flow stirred-tank reactor (CSTR) as an approximation of a plug flow reactor to describe limiting behavior without the effects of transport and inhomogeneity. However, this approximation is only suitable for the description of the plasma reactor due to the low nitrogen conversion. [38] The main advantage of this approach was that the original code did not need to be changed. Instead, ZDPlasKin solved the mass conservation of a batch reactor for each gas-phase specie by using Eq. 2[113]:

$$\frac{dn_i}{dt} = \frac{\Phi}{V} \bullet n_{i,0} - \frac{\Phi}{V} \bullet n_i + \sum_j r_{ij} \tag{2}$$

where a pseudo-species B_i was introduced for each of the gaseous species, following the pseudo-reaction $A_i \rightleftharpoons B_i$. The first-order forward reaction rate per volume unite was given as $\frac{\Phi N_i}{V}$, while the zeroth-order backward reaction was given as $\frac{\Phi N_{i0}}{V}$. After the system reaches an equilibrium state in a batch reactor, the net production rate of every species is zero. However, in the actual plasma reactor only a non-equilibrium steady state with non-zero production rates are reached, as there is a steady flow of reactant gas mixture into the system, as well as an outflow.[113] In a DBD system, a typical steady state cannot be achieved. Since a DBD is a periodic discharge, only a periodic steady state can be achieved where each discharge period becomes identical [34].

In kinetic models, plasma parameters serve as an input and are derived from plasma voltage and current characteristics, which can be influenced by the type of packing and catalytic surface, as well as the length of the outer electrode [34,39]. Plasma parameters are usually derived from experimental findings, current measurements and Q-U Lissajous diagrams and are treated as constants[17,29,113]. Therefore,

the kinetic models cannot predict the effects of current, frequency and charge transfer parameters. In order to investigate the effects of these parameters, a higher-dimensional model is needed, where the electric field and current would be computed self consistently[39].

3.1. Implementation of plasma properties

3.1.1. Plasma discharge regime

At atmospheric pressure, electron avalanches cause the formation of a space charge. This leads to an additional electric field that enhances the local growth of secondary electron avalanches causing rapid growth of the ionized region and the perturbation of the electric field, leading to the formation of distinct plasma channels. As these microdischarges are generated repeatedly, they appear visually as filaments.[115] In addition to filamentary microdischarges, surface microdischarges or surface ionization waves can also occur in fixed-bed DBD discharge, depending on the voltage waveforms[116]. However, under suitable conditions, more uniform plasma discharge can occur [41,117]. Van't Veer *et al.* [34,40] were the first to incorporate the spatial and temporal nature of microdischarges into the kinetic model for plasma-catalytic ammonia production. Microdischarges were defined as 200 ns long triangular pulses uniformly distributed over the residence time of the gas molecule, while afterglows were defined as a weaker plasma occurring in the time interval between the two consecutive microdischarges. Andersen *et al.* [39,118] also assumed a uniform distribution of microdischarges throughout the plasma volume, although the experimental current measurements showed that the occurrence of microdischarges was most frequent in the periods of voltage change from zero to its maximum/minimum value. This approximation was justified because a single molecule in the reactor does not have the opportunity to interact with all microdischarges, as its lifetime is short compared to the residence time of the gas in the DBD plasma system[34,40,119]. This especially applies to packed reactors, where residence times are even shorter[39]. A similar approach was later adopted by Engelmann *et al.* [8] and Liu *et al.* [120]. Since the plasma discharge can also have a mixed character with characteristics of both filamentary and uniform regime, a power distribution factor was introduced to implement all possible plasma regimes, as shown in Eq. 3.

$$P_{min} = \gamma_{dis} \bullet P_{max} \tag{3}$$

P_{min} is defined as the minimum power value, P_{max} as the maximum power value and γ_{dis} as the power distribution factor, which was originally set between 10^{-6}, indicating a fully filamentary regime, and 1, corresponding to a fully uniform plasma[34]. The value of the power distribution factor was determined based on the fit of the simulated to the experimental plasma power profile. Since the value 10^{-6} corresponded to a power of 540 W, Van't Veer *et al.* [34] set the minimum value of the power distribution factor to 0.1 in order to stay within a reasonable agreement with experimental power measurements[40]. Similarly, Andersen *et al.* [118] used experimentally determined microdischarge lifetime and power density profiles with different power distribution factors to model the microdischarges and found that the values 0.1 and 0.2 showed the best fit. Plasma regime has an influence on vibrational distribution function (VDF) and the radical densities. Engelmann *et al.* [8] carried out kinetic simulations in microdischarges and afterglows, as well as in a uniform plasma. A difference in vibrational distribution function (VDF) and radical densities was observed in microdischarges compared to afterglows. On the other hand, both remained approximately constant in the uniform plasma regime, leading to differences in surface kinetics. Peeters and van de Sanden[121] defined a non-discharging (α) and discharging (β) functions of the volume (Eq. 4 and 5) to account for the partial discharging of the non-noble gases when describing the plasma behavior. This scenario was later taken into account in the definition of burning voltage [34,39,113] used to determine the average plasma power $\overline{P}$(Eq. 6).[34,39,40,98]

$$\alpha = \frac{C_{diel} - \zeta_{diel}}{C_{diel} - C_{cell}} \tag{4}$$

$$\beta = 1 - \alpha \tag{5}$$

$$\overline{P} = 2 \bullet (1 + \frac{\alpha}{\beta} \bullet \frac{C_{cell}}{C_{diel}}) \bullet \Delta U \bullet \frac{Q_0}{1 - \frac{C_{cell}}{C_{diel}}} \bullet f_D \tag{6}$$

where C_{diel} is the dielectric capacitance, ζ_{diel} is the effective dielectric capacitance, C_{cell} is the reactor capacitance, ΔU is the burning voltage, Q_0 is the measured transferred charge and f_D is the discharge frequency. Assuming that all of the microdischarge peaks are the same height, Van't Veer *et al.* [34,40] and Andersen *et al.* [118] defined the average instantaneous maximum power $P_{inst.,max}$ (Eq.7), which consists of microdischarge pulses and a constant minimum power value, asigned as a uniform plasma component.

$$P_{inst.,max} = \frac{\overline{P}}{2 \bullet (1 - \gamma_{dis}) \bullet N_{MD} \bullet f_D \bullet \tau_{MD} \bullet \xi_s + \gamma_{dis}} \tag{7}$$

where τ_{MD} stands for the lifetime of the microdischarge, N_{MD} for the number of microdischarges per half cycle and ξ_s for the pulse shape factor, whose value is 0.5, which corresponds to a triangular pulse. The value of the plasma power is used to calculate the plasma power density and is treated as a constant determined from the experimental plasma characterization parameters, which serve as a model input. Van't Veer *et al.* [40] also defined the minimum(p_{min}) and maximum power density (p_{max}) in the periodic power density function (Eq.8). When defining the periodic microdischarge pulses, it was considered that an individual molecule cannot be exposed to all the microdischarges that take place throughout the entire reactor volume during the residence time of the molecule. As shown in Fig. 1, a modified pulse period $T_p^{\eta} = \frac{T_p}{\eta_{MD}}$ was used and the pulse was centered at $t_0^{\eta} = \frac{T_p^{\eta}}{2}$.

$$p^{\eta}\left(t_{mod}^{\eta}\right) = (p_{max} - p_{min}) \bullet \frac{2}{\tau_{MD}} \bullet max\left[(\frac{\tau_{MD}}{2} - \left|t_{mod}^{\eta} - t_0\right|, 0\right] + p_{min} \tag{8}$$

where η_{MD} is the fraction of microdischarges to which the individual molecule is exposed during its residence time, defined as the ratio between the discharge period and residence time of the molecule, and t_{mod}^{η} is the time at which the modified pulse takes place.

If all microdischarges taking place in the reactor are considered, the average power density $\overline{p}$ during the individual pulse period can be defined as the coefficient between the total plasma power and the discharge volume, which leads to Eq.9. The definition of the average power density $\overline{p}$ now consists of a microdischarge ($\left(1 - \gamma_{p.d.}\right) \frac{\tau_{MD}}{2T_p}$) and a uniform component ($\gamma_{p.d.}$).[40]

$$\overline{p} = \left[\left(1 - \gamma_{p.d.}\right) \bullet \frac{\tau_{MD}}{2T_p} + \gamma_{p.d.}\right] \bullet p_{max} \tag{9}$$

N_{MD} is the number of microdischarges per half cycle, τ_{MD} is the lifetime of the microdischarge, T_p is the pulse period, p_{max} is the maximum power density and $\gamma_{p.d.}$ is the power density distribution factor with values between 0 and 1 [40]. The same implementation of plasma regimes was used by Anderson *et al.* [39].

In order for ZDPlaskin to have a stable functionality, an approximation has to be made in which the reduced electric field and the electron density are treated as constants. This leads to the overestimation of ionic density to the point, where it is larger than the electron density. However, if reactions involving ions do not play an important role in the reaction mechanism, the approximation does not affect the simulation results.[29] Winter *et al.* [41] and Chen *et al.* [113] determined the reduced electric field strength by dividing burning voltage by the discharge gap and the total number density of gas
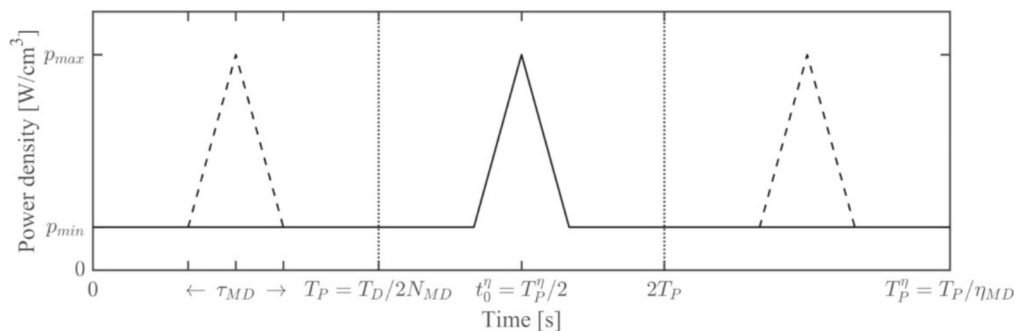
Fig. 1. Definition of the periodic microdischarge pulses. Reproduced with permission from ref [40]. Copyright © 2020 IOP Publishing Ltd.

molecules, while van't Veer *et al.* [31,40], Andersen *et al.*[39] and Liu *et al.*[120] used the assumption that E/N is not spatially dependent and computed the reduced electric field as a function of power density (Eq.10).

$$\frac{E}{N} = \frac{1}{N} \bullet \sqrt{\frac{p(t)}{\sigma}} \qquad (10)$$

Electron conductivity(σ) can be calculated as a function of electron density and electron mobility obtained from BOLSIG + . By using the electrical behavior from the experiments as input parameters, the models cannot predict the effects of parameters such as current, voltage and charge transfer. In order to achieve the self-consistent calculations of the electric field and current, a Poisson equation has to be solved, which requires higher-dimensional models.[39].

3.1.2. Plasma discharge volume

To obtain the values of the average plasma power, the volume of microdischarges and the uniform plasma have to be determined. The maximum power density corresponds to the maximum plasma power in the microdischarge and the microdischarge volume, while the minimum power density corresponds to the plasma power in the afterglow and the volume of the uniform plasma.[40] However, uncertainty about what fraction of the void volume is occupied by the plasma remains one of the challenges in plasma kinetic modeling[113]. Chen *et al.*[113] assumed that plasma occupies the entire void volume, but when the filamentary nature of the plasma discharge is considered, the volume of the microdischarge has to be defined. For the empty reactor Andresen *et al.* [39,118] modeled the volume of the microdischarge $V_{MD,empty}$ as a cylinder (Eq.11).

$$V_{MD,empty} = \pi \bullet gs \bullet r^2 \qquad (11)$$

where *gs* is the gap size and *r* is the radius of the microdischarge (reported to be in the order of 0.1 mm). For the packed bed reactor, the volumes of the microdischarge and the uniform plasma are defined separately by Eq.12 and Eq.13. [34,39]

$$V_{MD} = \frac{4\pi}{3} \bullet (0.29 \bullet r_{bead})^3 \qquad (12)$$

$$V_U = \beta_{p.d.} \bullet (1 - \alpha_{packing}) \bullet V_R \qquad (13)$$

r_{bead} is attributed to the packing bead radius, $\alpha_{packing}$ to the packing factor, which was set at 0.68, corresponding to a body-centred cubic structure, and $\beta_{p.d}$ to the partial discharging of the plasma reactor [34,39].

3.2. Influence of the packing material

Van't Veer *et al.* [31] used a particle tracing method to calculate the trajectories of gas molecules travelling through an empty and a full bed reactor. These results were later used as input to determine whether the

molecule was hit by a microdischarge while passing through the reactor (Fig. 2). It was found that molecules travelling through the center of the empty bed reactor have the highest velocity and shortest residence time, while in the packed bed reactor, the fastest molecules are passing right next to the reactor walls and are exposed to the least amount of microdischarges, as the local electric field and electron temperatures are enhanced near the contact points of the beads. [31,108,113,122].

A study of the plasma-modifying behavior of packed catalysts suggests that the catalyst may have a more important role as a plasma modifier in plasma-catalytic ammonia production, rather than its conventional role in surface chemistry. The catalyst can importantly influence the plasma discharge, which determines the predominant reaction mechanism. When the discharge has a more filamentary character, electron impact dissociation is of greater importance, whereas vibrational excitations appear to dominate in more uniform discharges.[83] Wang *et al.*[123] reported that in packed bed DBD reactor systems, the discharge is uniform when the dielectric constant of the packed material is below 5, and filamentary when the dielectric constant is above 1000. This is consistent with Feng *et al.*[81] who reported that packing the DBD reactor with γ-Al$_2$O$_3$ reduces the generation of filamentary discharges and results in a more uniform discharge. It is not known to what extent the constant is increased by loading with transition metals. However, Van't Veer *et al.* [34] and Chen *et al.* [113] reported no significant differences in plasma properties when Al$_2$O$_3$ beads with a dielectric constant of 9.3 were replaced with alumina beads impregnated with 5–10 wt% of transition metal. Recently, oxides with perovskite structures have emerged as a promising class of supports for plasma-catalytic ammonia production[84,124], as they enhance the electric field of the plasma region due to the high dielectric constant and additionally improve plasma-catalytic NH$_3$ synthesis through a strong
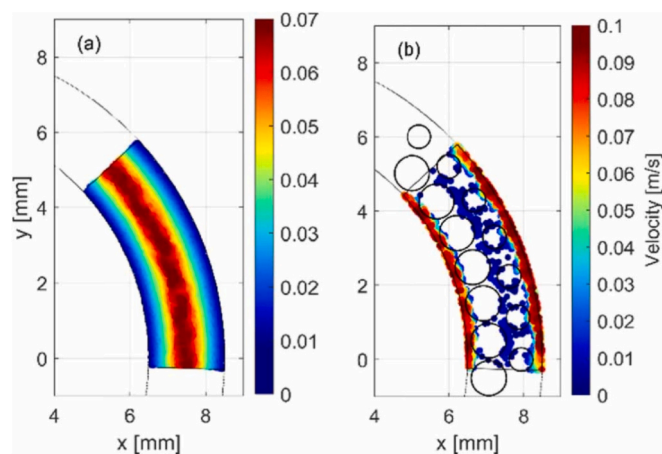

Fig. 2. Top view of the axial velocity of each particle in the empty (a) and packed bed (b) reactor. Reproduced with permission from ref [31]. Copyright © 2020 IOP Publishing Ltd.

metal-support interaction and oxygen vacancies that facilitate the adsorption and activation of N_2.[84,125,126] It has been reported that the microdischarge formation can also be promoted by zeolites, as they can influence the current–voltage properties of the plasma [9]. Chen et al.[113] suggested that ruthenium and copper nanoparticles on alumina promote microdischarge formation in DBD plasmas similarly to silver nanoparticles of Ag(10 wt%)/zeolite 13X [127]. Regardless it should be noted that the propagation of microdischarge formation over Ag/zeolite 13X might not only be the caused silver nanoparticles, but zeolite 13X as well. Patil et al.[128] on the other hand reported that manganese and iron inhibit plasma formation and generate low-energy discharges, resulting in poor performance compared to even plasma-only conditions, while more efficient metal catalysts showed no correlations with plasma generation. In addition, Andersen et al. [39,119] reported that ammonia dissociation rates over $Co/MgAl_2O_4$ are much lower compared to the support alone due to the weaker microdischarges, which significantly contributed to the increase in the overall ammonia synthesis rate. Contrary, the results of the sensitivity analysis performed by Chen et al.[113] showed that the molar fraction of ammonia is only 10 times lower when the Eley-Rideal reactions on ruthenium are ignored in the kinetic simulation, while the fraction is 7 orders of magnitude lower when the same reactions on alumina are ignored. These results suggest that alumina may have a stronger effect on ammonia production than metal nanoparticles. As evidence, it was reported that similar yields are obtained with a copper catalyst as with a ruthenium catalyst, even though their activity is different. Similar conclusions were drawn by Hong et al. [29] and others [29,32,44,62,128] who reported that surface reactions and radical adsorption can take place on non-metallic surfaces, such as alumina.[29] This was supported by DFT simulations, which showed similar energy profiles for N_2 activation with a high energy barrier for dissociation of adsorbed N_2 ground state, indicating that direct adsorption is the only pathway to produce adsorbed nitrogen atoms on MgO, Al_2O_3 and SiO_2 [17]. Van Raak et al. [129] observed the same effect, with the concentration of ammonia generated over CeO_2 being very similar to that over Ru/CeO_2. However, an 80.6 % increase in the maximum ammonia concentration was observed when the $Ti-CeO_2$ catalyst was substituted to $Ru/Ti-CeO_2$, indicating the importance of the strength of the metal-support interaction and the electronic metal-support interaction [129,130]. Metal nanoparticles also provide additional active sites for the adsorption of reactive species, leading to an increase in their local concentration [75]. Mehta et al.[38,44] demonstrated the contribution of metal nanoparticles in their microkinetic model by subtracting the rate of NH(s), NH_2(s), and NH_3 formation via the Langmuir-Hinshelwood mechanism over bare alumina from that calculated over the alumina-supported metal catalyst, resulting in the volcano-type dependence between nitrogen binding energy and ammonia turnover frequency. These findings explain the shift from the most active iron and ruthenium catalysts in thermal catalysis to cobalt and nickel catalysts in plasma catalysis for ammonia production.

In the last five years, many research groups have reported the improvement of ammonia formation by filling the DBD reactor with microporous materials such as zeolites [9,19,25,87], zeolitic imidazolate frameworks (ZIFs) [69,71] and metal–organic frameworks (MOFs) [131]. These catalysts improve ammonia synthesis by promoting diffusion of plasma-activated species to the active sites [9,19,35,78] and into the pores, as well as high specific surface area[19]. Gorky et al.[87] observed an increased ammonia production rate over SAPO-11 and SAPO-34 catalysts with pore sizes (3.9 and 3.8 Å) above the kinetic diameter of nitrogen (3.6 Å). However, the same effect was not observed when SAPO-56 with a pore size of 3.4 Å was used, indicating the importance of diffusion of active species inside the pores. On the other hand, the lifetime of reactive species is very short and their penetration depth is therefore only up to 1 µm.[25] Consequently, active species can access only the internal surface area near the external surface and the pore surface area towards the core plays no role in ammonia formation [35,113]. Nevertheless, Wang et al.[26] reported of shielding effect by

the MCM-41 support, where ammonia can diffuse into the pores and is consequently protected from dissociation in the plasma. However, this leads to only partial utilization of the active metal sites, as the reactive species are quenched before they reach the active sites in the pores. It has been reported that the efficiency of the metal active sites on porous support was improved by using an in-situ impregnation approach for catalyst preparation, which resulted in the majority of the active sites being located on the external surface of the support.[26] Zhang et al. [109] investigated the microdischarge behavior in the pores of the catalyst using a 2D fluid model for helium dielectric barrier discharge, which confirmed that plasma species can form inside the pores with a size larger than 10 µm. The increase in ammonia production by the porous catalyst was also demonstrated by Chen's[35] kinetic model. After replacing the non-porous glass with the porous SiO_2 catalyst, the H and N number densities increased by 78 % and 61 %, respectively, while the ammonia number density increased by up to 2.5 times. Nevertheless, it is important to note that the influence of a porous material was only considered in terms of an increased surface roughness, defined as a ratio between the accessible and external surface area. As mentioned before, porous supports can influence the plasma regime and the predominate reaction pathway. Further research into the synergy between plasma and packing material is required to potentially incorporate these effects into kinetic simulations, for example in the form of adjusted plasma powers and densities. Additionally, other computational methods, such as molecular dynamics, could be used to investigate the shielding effect of porous supports.

3.3. Plasma and surface chemistry

Due to the complexity of the reaction mechanism and the synergistic relationship between plasma and catalyst, a gap in understanding of the plasma-catalytic process presents an obstacle to improving its efficiency. Various reaction mechanisms have been proposed so far, as the reaction parameters and the choice of packing material can have an impact on the rates of important reactions. Mehta et al.[38] defined different reaction scenarios based on the rates of dissociative chemisorption of N_2, hydrogenation of adsorbed N species, and electron impact excitations. If the specific electrical energy input is too low or/and the bulk temperature is too high, thermal dissociation of N_2 takes place on catalyst surface. Since the rate of thermal dissociation exceeds the rate of N_2 excitation in the plasma, the reaction proceeds via the thermal catalytic pathway and the plasma has no beneficial effects. Homogeneous and heterogeneous plasma-catalytic reactions therefore become relevant when N_2 excitation rate is higher than the rate of its dissociative adsorption, while the hydrogenation of adsorbed N is not rate-limiting. At lower temperatures and low catalyst loading, the surface is saturated with adsorbed species, resulting in dissociative adsorption of excited N_2 molecules and subsequent hydrogenation of the adsorbed N to be slow compared to the formation of ammonia via gaseous reactions in the plasma. If the excitation of the N_2 molecules is not rate-limiting, the heterogenous reactions on the catalyst surface become less important compared to the homogeneous reactions inside the plasma.[38,44] Rouwenhorst[61] has identified 4 possible mechanisms for plasma-catalytic ammonia synthesis: plasma-phase (Fig. 3a), surface-enhanced plasma-driven (Fig. 3b), plasma-enhanced semi-catalytic (Fig. 3c) and plasma-enhanced catalytic (Fig. 3d).

The plasma-phase mechanism represents recombination of radical species to ammonia, independent of the catalytic surface. On the other hand, N and H species are directly adsorbed on the surface and subsequently quenched via Eley-Rideal reaction with the reactive species from the gas-phase or via Langmuir-Hinshelwood reaction with another adsorbed species in **the surface-enhanced mechanism**. Both mechanisms are limited by diffusion in either gas-phase or on the catalyst surface, as indicated by the fact that the reaction orders are 1 in N_2 and H_2 for both mechanisms.[10,61,132] In the **semicatalytic pathway**, hydrogen molecules are dissociatively adsorbed on the surface, whereas
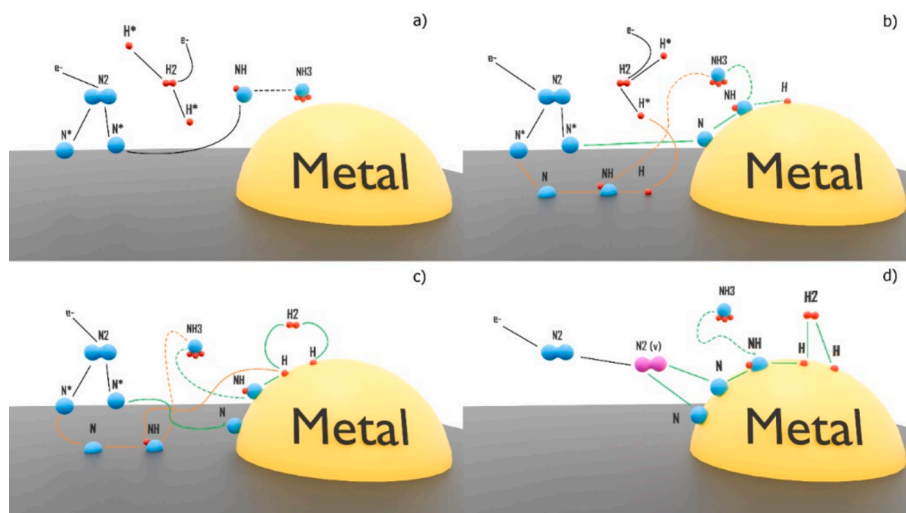
Fig. 3. Plasma catalytic ammonia synthesis mechanisms. Adapted with permission from ref [61]. Copyright © 2019 American Chemical Society.

nitrogen atoms formed in the plasma-phase are directly adsorbed on the surface. The reported orders for this pathway are 1 in N_2 and 0 in H_2, which is presumably a consequence of surface poisoning with hydrogen. [59,61] **Plasma-enhanced catalytic** mechanism is described as a pathway, in which H_2 and N_2 dissociatively adsorb on the catalyst surface. Due to the vibrational excitations in the plasma, the energy barrier of nitrogen triple bond dissociation is lower and thus susceptible to undergo dissociative adsorption on the surface. As the activation energy is strongly dependent on the catalyst, the orders can vary from one catalyst to another. Because the catalytic route is the most efficient, this is the preferred route for ammonia production. However, for it to be the dominant pathway, certain requirements have to be met in terms of reaction conditions, availability of active sites on the catalyst surface for dissociation of N_2 and operating temperatures. [61] Similarly, Bogaerts *et al.* [21] recognized the importance of promoting vibrational and electronic excitations over radical formation in the plasma, as excited gas species lower the dissociation energy barrier and thus improve the plasma-catalytic synergy.

Plasma kinetic modeling is a powerful tool to determine the optimal plasma conditions. To determine the dominant reaction pathway, typically more than 100 gas-phase and surface reactions of ground state molecules, vibrationally- and electronically excited molecules, atoms, ions as well as surface-adsorbed species, are considered.

3.3.1. Vibrational and electronic excitations

Excitations by electron collisions with gaseous species and relaxations of the excited species influence the electron energy distribution. As opposed to purely thermal conditions, where only vibrational excitations are accessible, plasma conditions promote electronic excitations, as well. These can promote surface reactions and enhance plasma kinetics by stimulating the formation of important intermediates or inhibit their composition along the undesired pathways. [21,29,117,133] As shown in Fig. 4, vibrational kinetics is particularly important in plasma chemistry at reduced electric field below 100 Td [134,135] where discharges have relatively low electron energies. On the other hand, relatively large amounts of energy can be stored in the form of vibrationally excited molecules with relatively long lifetimes. [29] Since vibrational excitation requires less energy compared to electronic excitations, ionizations, and dissociations, this is the main excitation mechanism in DBD plasmas [44]. For the catalytic reaction mechanism to be the predominant pathway for ammonia formation, the DBD plasma should be operated at lower reduced electric fields so that the vibrationally excited nitrogen molecules are abundant and radical species are quenched to either adsorbed NHx (x = 1,2,3) species or back to reactants on the catalyst surface [21,32]. However, this is usually not the case, as typical DBD plasmas operate at higher reduced electric fields, similar to the shaded regions in Fig. 4, which represent the energy
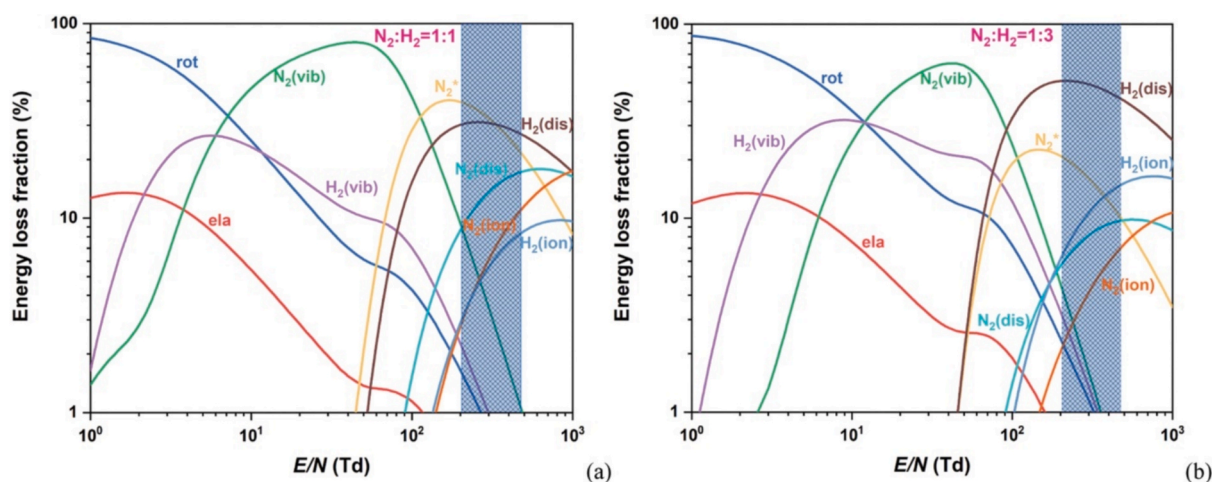

Fig. 4. Fractions of energy used by different excitation modes as a function of reduced electric field in (a) N_2:H_2 = 1:1 and (b) N_2:H_2 = 1:3 gas feedstock ratio (where ion stands for ionization, ela stands for elastic, rot for rotational, vib for vibrational and * for electronic dissociation – dis.). Reproduced with permission from ref [117]. Copyrights © 2022 IOP Publishing Ltd.

loss fraction due to different excitation modes between 204 and 475 Td. When vibrational excitations are not the dominant excitation route, the less energy-efficient radical-dominated reaction mechanisms become more important. [21,61].

A detailed description of vibrational and electronic kinetics, including vibrational-translational (V-T) relaxation, vibrational-vibrational (V-V) energy exchange between two identical molecules, and vibrational-vibrational (V-V') energy exchange between two different molecules, which have a significant impact on the vibrational energy distribution, has been implemented in many kinetic models [17,29,113,117,133]. The rates of V-T energy exchange are calculated by approximate relations based on Schwartz-Slawsky-Herzfeld (SSH) theory [29,117], which states that the most effective relative kinetic energy for causing a vibrational transition is much larger than the quantum of transferred energy. [43,136] The rate coefficient for the relaxation of the lowest excited vibrational level by V-T interaction can be expressed by Eq.14 as follows:

$$k_{1,0}^{VT} = A \bullet T_g^n \bullet e^{-\frac{B}{T_g^{\frac{1}{3}}} + \frac{C}{T_g^m}} \bullet \left[1 - D \bullet e^{-\frac{E_{1,0}}{T_g}} \right]^{-1} \qquad (14)$$

where T is the gas temperature, $E_{1,0}$ is the energy of transition from ground to first vibrational level, A, B, C, D, n and m are the fitting parameters. Similarly, the V-T relaxation coefficient of higher vibrational levels can be obtained from the relation (Eq.15):

$$k_{\nu+1,\nu}^{VT} = k_{1,0}^{VT} \bullet G(\nu+1) \qquad (15)$$

where ν is the vibrational level and $G(\nu + 1)$ is a scaling function, that can be calculated as a function of vibrational level, anharmonicity of the molecule, energy of vibrational transition from $\nu + 1$ to ν and reduced collision mass.[29] A detailed description of the determination of the value of scaling function and the reaction coefficients for V-V and V-V' exchanges can be found in the paper by Hong *et al.*[29]. Liu *et al.*[120] investigated the importance of different vibrational energy transfers on N and H number densities and NH$_3$ concentration by comparing 6 different models excluding specific vibrational energy transfer types to experimentally determined N and H number densities obtained *in-situ* via two-photon absorption laser-induced fluorescence.

The results showed that all types of vibrational energy transfer, including V-T relaxations, V-V exchanges, V-V' exchanges, and chemical abstraction processes, need to be included for the model to predict ammonia concentration well. When chemical abstraction reactions of vibrationally excited species were not included, the model underestimated ammonia concentration, while the concentration is overestimated when V-V exchanges or V-T relaxations were excluded. On the other hand, when V-V' exchanges were excluded, the prediction abilities of the model are comparable to the full model at voltages, lower than 14 kV. However, at higher voltages, the ammonia concentration is underestimated as discrepancy becomes more significant due to the increased production of vibrationally excited species. [120] The rate constants for the reactions, including the vibrationally excited species, can be calculated using the Fridman-Macheret α-model based on Eyring-Polanyi equation.[8,117,120,133,137] The rate coefficient for dissociative adsorption of a vibrationally excited nitrogen molecule is defined by Eq.16:

$$k_\nu = \frac{k_B \bullet T}{h} e^{\frac{\Delta S_L^{\circ \ddagger}}{R}} e^{-\frac{\Delta H_L^{\circ \ddagger}}{R \bullet T}} e^{\frac{\alpha_\nu \bullet E_\nu}{R \bullet T}} \qquad (16)$$

where E_ν is the energy of the vibrational level ν and α is the efficiency of the vibrational energy to lower the reaction barrier, the exact definitions of which are still unknown. Therefore, an approximate value defined by Fridman[8,138] is typically used instead (Eq.17):

$$\alpha_\nu = \frac{E_a^f}{E_a^f + E_a^b} \qquad (17)$$

E_a^f and E_a^b are the activation energy of forward and reverse reaction. If E_a^f is 0, the value of α is 0, which means that the reaction is limited by diffusion and the enthalpy barrier cannot be overcome. However, if E_a^b is 0 and α has a value of 1, the reaction is limited only by enthalpy and has the maximal benefit from the vibrational energy provided.[8,44,113].

Mehta *et al.* [44] identified the importance of vibrationally excited species in promoting the dissociative adsorption rate without affecting the subsequent reaction steps with their microkinetic model, which considered only the typical Haber-Bosch reaction and the dissociative adsorption of N$_2$ and H$_2$ without radicals. On the other hand, the kinetic calculations of van't Veer *et al.* [34] revealed that dissociative adsorption causes the initial coverage of N(s) and H(s) only at the very beginning of the synthesis, when a large amount of free surface sites is available, and N and H are present in small amounts. Morever, contribution of direct adsorption of N was already 98 %, even before the first microdischarge. The percentage even increased during the following microdischarges and afterglows. However, their model also showed that as soon as not all power is consumed by the microdischarges, vibrational excitations are important for promotion of nitrogen dissociation in both plasma regimes [40]. Engelmann *et al.*[8] studied the influence of VDF on the ammonia turnover frequency in vibrationally enhanced catalysis as a function of N* binding energy. In contrast to Mehta *et al.*[44] who assumed that VDF follows a truncated Treanor distribution at a vibrational temperature of 3000 K, Engelmann *et al.*[8] used explicitly calculated VDFs obtained from their plasma kinetic model. In addition to the effect of vibrational excitation, the effect of radical reactions was also investigated. As can be seen in Fig. 5, the turnover frequency showed a volcano-like relationship when only vibrational excitations were included in the simulation. Volcano plots were much wider for filamentary microdischarges and uniform plasma with higher maximum turnover frequencies shifted towards more noble metals. However, when radical adsorption and Eley-Rideal (E-R) reactions were included in the model, the shifts were overruled in both regimes and the typical volcano behavior was no longer observed, indicating that E-R reactions
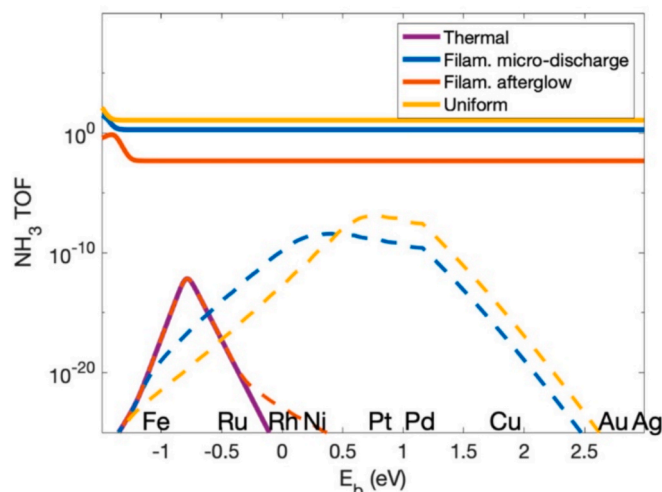

Fig. 5. Calculated ammonia turnover frequencies as a function of nitrogen binding energy for the metal terrace sites at 400 K and 1 bar in thermal catalysis (purple line), in microdischarges (blue line) and afterglows (red line) of a filamentary plasma regime, in uniform plasma (yellow line). The dashed lines represent the calculations, including only vibrational excitation. Reproduced with permission from ref [8]. Copyright © 2021 American Chemical Society. (For interpretation of the references to colour in this figure legend, the reader is referred to the web version of this article.)

and direct radical adsorption dictate the reaction pathways. [8,21] This was confirmed by the experimental results, as no significant differences in activity among the transition metals were observed [139].

3.3.2. Surface reactions

During plasma-catalytic ammonia production, various surface reactions take place, including adsorption, surface diffusion, Eley-Rideal (E-R) reactions, Langmuir-Hinshelwood (L-H) reactions and desorption [29]. Their rates are controlled by the adsorption energies of the intermediates and the activation energies of transformations from one adsorbed species to another [44]. The probability of surface reactions also depends strongly on the type of surface and available surface sites. The importance of surface reactions for the formation of ammonia was demonstrated by Chen *et al.* [113]. The results of their kinetic simulations showed that by excluding the surface reactions from the model, the molar fraction of ammonia is 7 magnitudes lower. Similar observations were made by van't Veer *et al.* [34], who reported that the ammonia concentration was 10 times lower when only gas-phase reactions were included in the model. The adsorption reaction rates as well as the hydrogenation rates can be estimated based on sticking coefficients for a given metal surface, support or reactor wall. Consequently, the sticking coefficient values influence the rate of the elementary surface reactions. Due to the lack of data on adsorption probabilities on different metal sites and supports, additional approximations about the surface properties, number of sites for adsorption of species and accessibility of these sites have to be made, which leads to the uncertainties of the models. [34,39,119] Typically, plasma kinetic models do not consider surface modifications or the solubility of the gases in the bulk surface and predict only monolayer adsorption [140]. If the products of the surface reactions are stable molecules such as N_2, H_2 or NH_3, their spontaneous desorption is considered in the reaction kinetics, while the surface-adsorbed intermediates (H(s), N(s), NH(s) and NH2(s)) remain on the surface [29,140,141].

3.3.2.1. Wall relaxations.

Although the effect of the catalyst surface area reportedly overcomes the wall effect (different excitation behavior and reaction rates due to the interaction with the walls of the reactor and decay)[74,140], the relaxation of excited species at the walls of the reactor is usually considered in plasma kinetic models [29,35,40,42,113,117,133,140]. The rate coefficient of relaxation of excited species by interaction with the surface k_{wall} can be expressed by Chantry's formula [142] (Eq.18):

$$k_{wall} = \left[\frac{\Lambda^2}{D} + \frac{V_R}{A_{eff}} \frac{2 \bullet (2 - \gamma_{wall})}{\bar{\nu} \bullet \gamma_{wall}} \right]^{-1} \tag{18}$$

where γ_{wall} is the wall loss probability, Λ is the diffusion length ($\frac{R_r}{2.405}$ for an empty reactor and $\frac{0.2R_r}{2.405}$ for a reactor packed with catalyst, while R_r is the inner radius of the reactor tube[143]), D is the diffusion coefficient (calculated from the Fuller–Schettler–Giddings equation [113,144] or using the Chapman-Enskog approximation[37,143]), V_R is the reactor volume, A_{eff} is the effective surface area and $\bar{\nu}$ is the thermal velocity obtained from Eq.19[40,42].

$$\bar{\nu} = \sqrt{\frac{8 \bullet k_b \bullet T}{\pi \bullet M}} \tag{19}$$

k_b is the Boltzmann constant; T is the temperature and M is the molecular weight of the species.

Due to the important role of reactions of ionic species in the RF plasma, Shah *et al.*[140] included the neutralization of ions on the reactor walls and the Fe catalyst in their kinetic model. The calculation of the reaction rate coefficients (Eq.20) was based on the difference between the total ion density generated by the electron impact ionization reaction and the ion density lost due to electron–ion recombination, which was balanced by the total ion flux to the walls/Fe catalyst surface

in order to meet the electroneutrality condition.

$$k_{wall\ neut.} = \frac{\sum_j R_j^X - \sum_k R_k^E}{\sqrt{m_l} \left(\sum_{10}^{l=1} \frac{|z_l|}{\sqrt{m_l}} \right)} \tag{20}$$

$[z_l]$ is the density of ionic species, R_j^X the rate of electron impact ionization, R_k^E the rate of electron–ion recombination and m_l the mass of the lost ion.

3.3.2.2. Direct radical adsorption.

Direct adsorption of atoms from the gas phase plays an important role in the formation of surface adsorbed precursors for ammonia production at atmospheric pressure [10,41,44]. When N, H and NH_x radicals with higher reaction energies compared to ground state species interact with the catalyst surface, a direct adsorption process with the rate coefficient k_{ads} can occur. The values of the coefficients are strongly influenced by the surface properties.[29,117] Hong *et al.* [29] assigned one of the empty surface sites as one of the reactants in the direct adsorption of radical species, which would lead to the formation of the surface adsorbed species N(s), H(s) and NH_x(s). Due to the adsorption reaction, the gas-phase reactant is lost, which can be described by the following rate equation Eq.21[29]:

$$\frac{d[Y]}{dt} = -k_{ads} \bullet \left(S_F - \sum X(s) \right) \bullet [Y] \tag{21}$$

where Y represents the radical in plasma, S_F the available empty surface and $X(s)$ the adsorbed species. With the use of rate equation, the adsorption reaction coefficient k_{ads} was defined by considering a decay time of the gas-phase species by diffusion and adsorption loss at the surface as follows (Eq.22) [29]:

$$k_{ads} = \left[\frac{\Lambda^2}{D_{diff}} + \frac{V_R}{A_{eff}} \frac{2 \bullet (2 - \gamma_{ads})}{\bar{\nu} \bullet \gamma_{ads}} \right]^{-1} \bullet S_T^{-1} \bullet \left(\frac{V}{A} \right) \tag{22}$$

With Λ representing the diffusion length, D_{diff} the diffusion coefficient, V_R the reactor volume, A the effective surface area, S_T the total surface site density (10^{15} cm^{-2} based on a nonspecific metal surface representation[145]), γ_{ads} the adsorption probability (sticking coefficient), $\bar{\nu}$ the thermal velocity and $\frac{V}{A}$ the ratio between the volume and the surface area of the reactor, which is added to convert the rate coefficients to the suitable measure unit.[35,113] Similar approach was often used in other kinetic models[17,41,42,113,140]. When calculating the effective surface area, surface roughness is considered. Winter *et al.* [41] determined the roughness factor (r.f.) for metal loaded catalyst supports in the form of a powder from experimentally determined parameters in Eq.23.

$$r.f. = m_{catalyst} \bullet S_{BET} \bullet w_{metal} \tag{23}$$

$m_{catalyst}$ is the catalyst mass, S_{BET} the specific surface area, determined by the BET method, and w_{metal} is the metal loading. The exact definition was implemented into the model by Pan *et al.* [42] and Chen *et al.* [35,113]. However, the latter defined effective surface area as equation Eq.24, resulting in enhanced rate constants for E-R reactions and direct radical adsorption with increasing surface area and higher surface accessibility:

$$A_{actual} = A_{external} \bullet (1 + L_i \bullet \rho_p \bullet S_p) \tag{24}$$

L_i is the penetration length of species i, which is computed by using Eq.25[113], ρ_p the particle density, S_p the surface per mass of the particle, D_{ie} the effective diffusivity and τ_i the lifetime of the particle i, which is described with Eq.26[113].

$$L_i = \sqrt{D_{ie} \bullet \tau_i} \tag{25}$$

$$\tau_i = \frac{N_i}{\sum_j r_{ij}} \tag{26}$$

where N_i is the number density of the specie i and r_{ij} is the rate of

reaction j, that quenches species i. Using this definition of effective surface area, the values of V/A obtained were between 10^{-6} and 10^{-5} cm. However, their sensitivity analysis showed that decreasing V/A lower than 0.001 cm (where the molar fraction of ammonia is 2.5 times higher than at V/A = 0.018 cm) does not significantly increase the ammonia formation rate. On the other hand, at a V/A value of 10^{-5} cm, the system is much more sensitive to changes of the sticking coefficients. Following Hong[29] and Carrasco[141], Chen et al.[113] set the value of the sticking coefficient on a metallic surface to 1 for all atoms and radicals. The same value was used by Shah et al.[140] for the Fe surface, while the sticking coefficient of 0.18 was chosen for the adsorption of N and 0.018 for the adsorption of H, NH and NH$_2$ on quartz reactor wall. Similar to Hong et al.[29], the chosen value for H was an order of magnitude lower compared to the other species to avoid a large overestimation of the H(s) and underestimation of the N(s) species, which would lead to a lower ammonia yield compared to the experimental results.[140] To account for the different sticking coefficients of N on quartz and Fe, Shah et al. [140] implemented effective reaction probabilities (Eq.27), which are defined as a combination of the corresponding values and consider the relative combination of the two different surfaces:

$$\gamma_{eff} = \gamma_{wall\ mat.} \times \frac{l_{wall}}{l_{wall} + l_{catalyst}} + \gamma_{catalyst} \times \frac{l_{catalyst}}{l_{wall} + l_{catalyst}} \quad (27)$$

where $\gamma_{wall\ mat.}$ and $\gamma_{catalyst}$ are the reaction probabilities for the pure wall material and pure Fe catalyst, respectively. l_{wall} and $l_{catalyst}$ are the lengths of the reactor tube and the Fe catalyst in the discharge plasma region observed from the experiments. The equation was used to compute the effective reaction probability of E-R reactions, recombination-surface desorption reactions and dissociative adsorption. As the reaction probabilities for direct adsorption of H, NH and NH$_2$ were 1 order of magnitude lower compared to N, Eq. (27) is no longer suitable, because it leads to high overestimation of the effective reaction probabilities and underestimation of the ammonia yield. Therefore, the equation was modified as follows (Eq.28):

$$\frac{1}{\gamma_{eff}} = \frac{1}{\gamma_{wall\ mat.}} \times \frac{l_{wall}}{l_{wall} + l_{catalyst}} + \frac{1}{\gamma_{catalyst}} \times \frac{l_{catalyst}}{l_{wall} + l_{catalyst}} \quad (28)$$

Sun et al.[117] computed the adsorption reaction coefficient using a simplified expression based on kinetic theory of gases combined with the surface chemistry principles (Eq.29).

$$k_{ads} = \gamma_{ads} \frac{\prod_{j=1} \theta_j^{\nu_{jr}}}{S_T} \sqrt{\frac{R \bullet T}{2 \bullet \pi \bullet M}} \quad (29)$$

Where θ_j is the number of sites that the surface adsorbed species j occupies, S_T is the total surface site density, ν_{jr} is the order of reaction r for species j, R is the universal gas constant and M is the molecular weight of the gas species.

3.3.2.3. Eley-Rideal reactions. Due to the high number of radical species in the gas phase, it is not surprising that Eley-Rideal (E-R) reactions between the radical species in the plasma phase and adsorbed species is an important hydrogenation mechanism in plasma-catalytic ammonia production [51]. The occurrence of E-R reactions on metal surfaces was proven theoretically by *ab initio* molecular dynamics studies of radio-frequency-driven N$_2$-H$_2$ plasma at 300 K[146] as well as experimentally by isotope labeling experiments[147]. In addition, Zhao et al.[148] detected N$_2$H$_y$ species as side products by *in-situ* Fourier Transform Infrared Spectroscopy and molecular beam spectroscopy, whose presence could only be explained by the E-R reactions. Similar to the adsorption rate coefficient, Sun *et.al* [117] defined the E-R reaction rate coefficient k_{ER} as described by Eq.30, while others[17,29,35,113,140] used Eq.31, which is derived from collision theory.

$$k_{ER} = \gamma_{ER} \frac{\prod_{j=1} \theta_j^{\nu_{jr}}}{S_T} \sqrt{\frac{R \bullet T}{2 \bullet \pi \bullet M}} \quad (30)$$

$$k_{ER} = \left[\frac{\Lambda^2}{D_{diff}} + \frac{V_R}{A_{eff}} \frac{2 \bullet (2 - \gamma_{ER})}{\overline{\nu} \bullet \gamma_{ER}} \right]^{-1} \bullet S_T^{-1} \bullet \left(\frac{V}{A} \right) \quad (31)$$

Where γ_{ER} is the E-R reaction probability. Both approaches are based on modeling of E-R reactions through sticking coefficients, although modeling through an energy barrier can also be applied [95]. Hong et al. [29] assumed that the value of E-R reaction probability is 10 times lower on than on non-metallic surface. The same approximation was made by Chen et al.[113] who implemented the same values for metallic sites as Carrasco *et al.*[141]. In kinetic and microkinetic simulations, an approximation is often made that all metals have the same activity for not only E-R reactions but also for other surface reactions. While Engelmann et al.[8] presented good agreement of their microkinetic simulations with experimental observations, DFT-based study by Michiels et al.[95] suggested that the metal influences the E-R reaction probability. However, in order to definitively determine the influence of metal type, *ab initio* molecular dynamics studies are required [95]. Although E-R reactions are important for the formation of ammonia, they also have a large impact on the energy efficiency of ammonia production, as the E-R recombination to original gasses also take place on the catalyst surface. The E-R recombination probabilities on metallic surfaces can be easily obtained from the literature, but the data for non-metallic surfaces are scarce. Since the values are highly dependent on various parameters such as the species type, gas composition, plasma characteristics and surface properties, some assumptions must be made to determine them [140]. The ratio between the assumed N and H adsorption probabilities has a major influence on the recombination rates and thus the ammonia yield. Chen et al. [113] identified possible reasons for the low energy efficiency of plasma ammonia synthesis by calculating the utilization rate of hydrogen (Eq.32) and nitrogen radicals (Eq.33).

$$utilization\,rate\,of\,H = \frac{3R_{NH_3}}{R_{H,prod}} \quad (32)$$

$$utilization\,rate\,of\,N = \frac{R_{NH_3}}{R_{N,prod}} \quad (33)$$

where $r_{NH_3,prod}$ is the total ammonia production rate, $r_{H,prod}$ is the total atomic hydrogen production rate of reactions that do not include NH$_x$ and NH$_x^+$ as reactants and $r_{N,prod}$ is the total atomic nitrogen production rate of reactions that do not include NH$_x$ and NH$_{xy}^+$ as reactants. The simulation showed that the utilization rate of H is only 13 %, while the utilization rate of N was determined to be 83 %.[113] However, it should be noted that the fraction of dissociated N$_2$ is much lower than the fraction of dissociated H$_2$. The reason for the low hydrogen utilization rate is mostly the E-R recombination of H(s) to hydrogen molecules, which not only consumes H atoms but wastes energy. However, Winter et al.[41] found that high recombination coefficient of adsorbed H on Ni contributes to the higher activity of the Ni catalyst, as hydrogen recombination leads to a higher density of available active sites for the adsorption of nitrogen atoms. A higher concentration of adsorbed NH$_x$ also indicates a lower recombination coefficient of the adsorbed nitrogen as well as a more effective hydrogenation of the adsorbed NH$_x$ species. In contrast, Liu et al.[32] found the recombination of nitrogen to be more favorable on all investigated metals (Au, Sn, Ag, Pd, Ni, Cu, Ga and Fe) based on the DFT calculations, which is another reason for the hydrogen poisoning of the catalyst surface. Even though Langmuir-Hinshelwood recombinations are possible, the Eley-Rideal mechanism is usually more dominant.[39,113,149].

In contrast to the Langmuir-Hinshelwood reactions, which have been researched in terms of the Haber-Bosch process[30,150–153], there have been very few fundamental studies on E-R reactions in plasma catalysis. Michiels et al.[95] were the first to systematically study E-R reactions for plasma catalysis. The intersections of a potential energy surface for a series of E-R reactions involving gas-phase H were

constructed as a function of height relative to the adsorbate based on DFT studies. This approach provided a computationally cheaper alternative to *ab initio* molecular dynamics studies (AIMD). It was found that kinetic models often overestimate the importance of E-R reactions, because the determination of the E-R reaction probabilities does not account for important factors, such as coverage, adsorbate type and sterical hindrance. It has been proposed that rate coefficient of E-R should be set to 0 if the coverage is below a certain coverage threshold of the specific surface reaction, since direct adsorption or even the hot atom mechanism, which is mostly not even considered in kinetic models, are more likely to occur if the free space is available in proximity of the adsorbate with sterical hindrance. This is in agreement with Galparsoro [154] who studied the importance of stereodynamics on E-R reactions using adiabatic and nonadiabatic quasiclassical molecular dynamics and found that sterical hindrance plays an important role, especially for N.

3.3.2.4. Langmuir-Hinshelwood reactions. In computational descriptions of plasma-catalytic ammonia synthesis, Langmuir-Hinshelwood (L-H) reactions are often either assigned a minor role or omitted altogether due to high activation energy and low concentrations of N(s) species [29]. Chen *et al.*[113] reported that these reactions do not significantly contribute to ammonia production on alumina surface. However, the results of their kinetic simulations of NH(s) formation on Ru sites at different values of reduced electric fields showed that the L-H pathway becomes more dominant at lower E/N values. Reduced E/N leads to lower electron temperatures, which causes a drop in number densities of the major gaseous precursors, leading to a decrease in E-R reaction and direct adsorption rates [113]. In contrast to other published works [17,29,34,113,140], Sun *et al.*[117] identified the L-H reactions of $NH_x(x = 0,1,2)$ with H(s) as crucial for ammonia formation. They suggested that N_2 and H_2 may also be formed via the L-H mechanism, which was not reported in the other studies mentioned. Shah *et al.*[140] did not include the L-H recombinations in their kinetic model because of the low contributions of recombinations to H_2 and high activation barrier for diffusion of N(s) species. The L-H reaction rate coefficient k_{LH} can be calculated from Eq.34.

$$k_{LH} = \frac{\nu}{4 \bullet S_T} \bullet e^{\frac{E_d + E_a}{k_B \bullet T_{wall}}} \bullet S_T^{-1} \bullet \left(\frac{V}{A}\right) \tag{34}$$

where ν stands for the surface diffusional jump frequency (10^{13} s^{-1} [141]), E_d for the diffusion energy barrier (0.2 eV for metal site[140], 0.5 eV for alumina[29,42] and quartz[140]), E_a for the activation energy and T_{wall} for the temperature on the surface. [29,42,140] T_{wall} is usually considered equal to the gas temperature, as the equilibration times of the surface reactions are long enough to conclude that the heat transfer between the gas and the surfaces is sufficient before the concentration of both species reach steady state [29]. Shah[140] approximated the diffusion energy barriers for different surfaces using Eq.35.

$$E_{deff} = E_{dwallmat.} \times \frac{l_{wall}}{l_{wall} + l_{catalyst}} + E_{dcatalyst} \times \frac{l_{catalyst}}{l_{wall} + l_{catalyst}} \tag{35}$$

3.3.2.5. Dissociative adsorption. Dissociative adsorption does not have a significant influence on the ammonia formation rate at low pressure, however it has a more fundamental role at higher total pressures and in thermal catalytic synthesis [29,41,140]. It was proved by isotopic exchange that in a DBD atmospheric pressure plasma dissociative adsorption on the surface takes place[155] and was even considered the main source of N(s) and H(s) species. The kinetic simulations, however showed that in a DBD plasma system, dissociative adsorption controls the surface coverage with N only during the first couple of pulses, while direct adsorption of N becomes more prominent in the later pulses due to the occupancy of the surface with H. Although the kinetic models showed that direct adsorption of N was responsible for more than 80 % adsorbed N(s), a significant kinetic effect of dissociative adsorption of

vibrationally excited nitrogen molecules on the formation of N(s) was found.[34,40,117] Chen *et al.* [35,113] did not include dissociative adsorption of nitrogen molecules in their kinetic model as it was considered unlikely on oxides such as alumina. Kinetic simulations of the same model at various E/N and mean electron temperature values, demonstrated that the importance of dissociative adsorption of vibrationally excited nitrogen on Ru sites decreases at lower E/N and mean electron temperatures. The combination of optimal E/N and mean electron temperature, at which dissociative adsorption of nitrogen molecules would be enhanced and the formation of N and H radicals in the gas phase would be minimized, was not identified with their kinetic simulations.[113] In plasma kinetic models the rate coefficients of dissociative adsorption $k_{diss.ads.}$ are determined by one of the following equations. The most commonly used Eq.36 is expressed in the same way as the rate coefficients of other surface reactions, with the difference in the sticking coefficient and inverse proportion to the square value of the total surface site density accounting for the formation of 2 new surface species [40,42,140]. The same approach to determine the rate coefficient of dissociative adsorption was used by Sun *et al.* [117,133](Eq.37). Hong *et al.*[37] described the dissociative adsorption of N_2 by deriving the activation energy of N_2 dissociation from DFT calculations and treating it as a 2-step process, described by Eq.38. The first step is the adsorption of N_2 on the surface of the catalyst, followed by the dissociation process. This correction led to a 1.2 % decrease in ammonia production rate, as the density of N(s) is overestimated in the conventional models [37].

$$k_{diss.ads.} = \left[\frac{\Lambda^2}{D_{diff}} + \frac{V_R}{A_{eff}} \frac{2 \bullet (2 - \gamma_{diss.ads})}{\bar{\nu} \bullet \gamma_{diss.ads}}\right]^{-1} \bullet S_T^{-2} \bullet \left(\frac{V}{A}\right)^2 \tag{36}$$

$$k_{diss.ads.} = \gamma_{diss.ads.} \frac{V_R}{A_{eff}} \frac{\prod_{j=1} \theta_j^{\gamma_{jr}}}{S_T^2} \sqrt{\frac{R \bullet T}{2 \bullet \pi \bullet M}} \tag{37}$$

$$k_{diss.ads.} = k_{ads} \bullet k_{L-H} = \frac{\upsilon}{4 \bullet S_T^2} \left[\frac{\Lambda^2}{D_{diff}} + \frac{V_R}{A_{eff}} \frac{2 \bullet (2 - \gamma_{ads})}{\bar{\nu} \bullet \gamma_{ads}}\right]^{-1} \bullet e^{\frac{-(E_d + E_a)}{k_B \bullet T_{wall}}} \tag{38}$$

The sticking probability or the probability of dissociative adsorption $\gamma_{diss.ads.}$ is determined as a function of the kinetic energy and the vibrational level of the H_2 and N_2 molecules (Eq.39)[40,156–158].

$$log_{10}(\gamma_{diss.ads.}(E_{kin}, \nu)) = a_\nu + b_\nu \bullet (1 - e^{-c_\nu \bullet E_{kin}}) + (1 - e^{-d_\nu \bullet E_{kin}}) \tag{39}$$

where E_{kin} is the kinetic energy and ν is the vibrational level of gas molecules colliding with the catalyst surface, while a_ν, b_ν, c_ν and d_ν are the fit parameters. Van't Veer *et al.*[40] used an average value of the sticking coefficient for dissociative adsorption of ground state and vibrationally excited nitrogen molecules, calculated by using Eq.40, where $P(E_{kin})$ is the probability distribution function defined as described in Eq.41.

$$\bar{\gamma}_{diss.ads.}(N_2) = \frac{\int P(E_{kin}) \bullet \gamma_{diss.ads.}(E_{kin}, \nu)dE_{kin}}{\int P(E_{kin})dE_{kin}} \tag{40}$$

$$P(E_{kin}) = \frac{1}{\sqrt{2 \bullet \pi \bullet M(N_2) \bullet k_B \bullet T_g}} \bullet \sqrt{\frac{E_{kin}}{k_B \bullet T_g}} \bullet e^{-\frac{E_{kin}}{k_B \bullet T_g}} \tag{41}$$

Liu *et al.*[32] even found a non-dissociative adsorption of N_2 and H_2 in their DFT studies of the plasma-catalytic system. When the nitrophilicity of the metal was high enough (in case of Pd, Co, Ni and Fe), the adsorption of N_2 changed from physisorption to chemisorption. On the other hand, H_2 was physisorbed at all metal sites except for Pd, where H_2 was chemisorbed by adopting a horizontally bound position on a top site, and Fe where it was spontaneously dissociated at the surface.

4. Determination of the main production/loss mechanisms of important reactive species

Kinetic models can predict the time evolution of the density or concentration of species considered in the included reactions, making them an important tool for determining the dominant reaction pathways and rate-limiting steps. Reported simulations were carried out for different reaction conditions, plasma power sources and packing materials, which all importantly influence the reaction pathways. Therefore, the main production and loss mechanisms of important gas-phase and surface species presented in the following chapter serve as an overview of different reaction pathways proposed based on experimental and computational research. The conditions under which the most frequently considered simulations were carried out are summarized in Table 2.

4.1. NH

Gas-phase NH is considered a crucial species in plasma-catalytic ammonia production, especially in plasma-only systems, as it is the main precursor for gas-phase ammonia formation via three-body reactions(reactions R(1) and R(2) [29,34]. Hong *et al.*[29] reported that three-body reactions are important during the early stage of the reaction, even in packed-bed reactor system, while others[34,117] later found them to contribute little to ammonia production and only have significant importance in plasma-only production. Several main formation mechanisms of NH in packed-bed plasma-reactor systems have been proposed instead, with their relevance depending on the specific reaction conditions. As already discussed in **chapter 3.3.1**, vibrational kinetics is particularly important in plasma chemistry at a reduced electric field below 100 Td. As typical DBD plasmas operate at higher reduced electric fields, reaction R(3), involving electrically excited hydrogen molecules, is generally identified as the main source of NH [47,117]. Sun *et al.*[117] also reported a significant contribution from reaction R (6). Kinetic simulations performed by Van't Veer *et al.*[34] and Andersen *et al.*[39] also showed that reaction R(3) is crucial in microdischarges when the plasma is more powerful and reduced electric field was higher than 100 Td. On the other hand, Hong[29] and Liu[120] found that vibrationally excited hydrogen molecules played a more significant role (reaction R(4) in the early stage of ammonia synthesis, compared to the electronically excited precursors. However, near the steady state, when the concentration of ammonia was higher, its dissociation by collision with electrons (reaction R(5) became the main source of NH [29,34,39,47]. In low-pressure plasma systems, other reactions are dominating, such as the gas-phase collision of H with NH_2 (reaction R (7).

$$NH + H_2 + H_2 \rightarrow NH_3 + H_2 \tag{R1}$$

$$NH + H_2 + N_2 \rightarrow NH_3 + N_2 \tag{R2}$$

$$N + H_2(E) \rightarrow NH + H \tag{R3}$$

$$N + H_2(v) \rightarrow NH + H \tag{R4}$$

$$NH_3 + e^- \rightarrow NH + H_2 + e^- \tag{R5}$$

$$N(E) + NH_3 \rightarrow NH + NH_2 \tag{R6}$$

$$H + NH_2 \rightarrow NH + H_2 \tag{R7}$$

As a precursor, NH is mostly converted to the surface-adsorbed species NH(s) by direct adsorption (reaction R(8)[39] and NH_2(s) by the E-R reaction R(9)[29,34,39,42,47,117]. In some cases reactions R10 [29] and R11[117] were also suggested to have a sufficiently large contribution to NH consumption.

$$NH + surf \rightarrow NH(s) \tag{R8}$$

$$NH + H(s) \rightarrow NH_2(s) \tag{R9}$$

$$NH + H \rightarrow N + H_2 \tag{R10}$$

$$NH + H_2 \rightarrow H + NH_2 \tag{R11}$$

4.2. H(s)

The surface-adsorbed hydrogen atoms are the main surface species and play a vital role in ammonia production. Since the bond strength of hydrogen molecules is much lower compared to nitrogen molecules, both H(s) formation mechanisms have a higher reaction rate compared to N(s), which leads to the saturation of the metal active sites with H(s) [29,34,39]. For this reason, a N_2/H_2 ratio of 1 or 2 is often used for plasma-catalytic ammonia production instead of the conventional 0.33 ratio[9,26,56,61,62,67–69,75,77]. The dominant H(s) production reaction is pressure-depending. Modeling results generally showed dissociative adsorption to be dominating at atmospheric pressure [29,42,47,117], where vibrationally excited H_2 has a minor role, while direct adsorption of gas-phase H is more important at lower pressures [113,140]. Contrary, Van't Veer[34] and Andersen[39] found that dissociative adsorption is a more important source of H(s) only before the first microdischarge, when the number density of empty surface sites is still high and is later replaced by radical adsorption. H(s) was also reported to be the only species consumed during the microdischarges and produced during the duration of the afterglows. Because the number density of gas-phase H is high during microdischarges, H(s) is easily recombined to H_2.[34,39]

$$H_2 + 2 surf \rightarrow 2 H(s) \tag{R12}$$

$$H + surf \rightarrow H(s) \tag{R13}$$
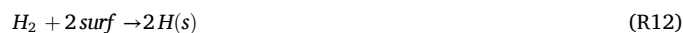
Unlike H(s) production mechanism, the consumption mechanism is

Table 2
Reaction conditions in modelling simulations of plasma-catalytic ammonia synthesis.

Model type	Plasma discharge type	Pressure	Temperature [K]	E/N [Td]	Packing material	Reference
kinetic	DBD	atmospheric	400	30–70	Al_2O_3	[29]
kinetic	DBD	atmospheric	400	1–10 in a.g. 140 in m.d.	spherical beads	[40]
kinetic	DBD	atmospheric	400	6 in a.g. 105 in m.d.	Al_2O_3	[34]
kinetic + DFT	DBD	atmospheric	500	82.3	SiO_2	[37]
microkinetic + DFT	DBD	atmospheric	400	20–100	Ru; Cu; Ni	[8]
kinetic	DBD	550 torr	523	142; 141	Al_2O_3; Ru/Al_2O_3	[113]
kinetic	DBD	atmospheric	473–483	–	$MgAl_2O_4$; $Ru/MgAl_2O_4$; $Co/MgAl_2O_4$	[39]
kinetic	RF	0.26 torr	673	–	Fe wire	[140]
deep learning-assisted pulsed discharge plasma-catalytic	DBD	atmospheric	293–773	80–110	Ru/MgO	[42]
kinetic	DBD	100 torr	340–360	1–200	–	[120]

not as straight forward. Based on kinetic simulations, many different consumption reactions were identified as important. In addition to the recombination to H_2 (reaction R14), E-R reactions with NH_x (x = 0,1,2) R9, R14, R15, R16 and R17 are commonly reported to be the major source of H(s) consumption[29,34,37,39,42,47]. However, Sun[117] and Shah[140]determined, that H(s) is mainly consumed via L-H reactions R18, R19 and R20 with NH_x(s) species. It has to be noted that Sun[117] computed the rate coefficients of direct radical adsorption and E-R reactions from a simplified expression based on kinetic theory of gases combined with the surface chemistry principles while others used the expression derived from collision theory and that Shah[140] used his model to simulate the reaction in the RF plasma discharge, while others simulated the reaction in the DBD plasma discharge. Additionally, recombination to H_2 via L-H mechanism (reaction R21) is possible, however its significance to H(s) consumption is much smaller compared to the E-R recombination[39].

$$H + H(s) \rightarrow H_2 + 2\,surf \tag{R14}$$

$$N + H(s) \rightarrow NH(s) \tag{R15}$$

$$NH_2 + H(s) \rightarrow NH_3 + surf \tag{R16}$$

$$N(E) + H(s) \rightarrow NH(s) \tag{R17}$$

$$N(s) + H(s) \rightarrow NH(s) + surf \tag{R18}$$

$$NH(s) + H(s) \rightarrow NH_2(s) + surf \tag{R19}$$

$$NH_2(s) + H(s) \rightarrow NH_3 + 2\,surf \tag{R20}$$

$$H(s) + H(s) \rightarrow H_2 + 2\,surf \tag{R21}$$

4.3. N(s)

The species N(s) can be produced by either dissociative adsorption of ground state or vibrationally excited nitrogen molecules (reactions R22 and R23) or by direct adsorption of gas-phase N atoms (reaction R24) obtained by dissociation of N_2 in plasma. The latter has often been identified as the main N(s) formation mechanism by plasma-(micro) kinetic modeling simulations[8,34,37,113,140]. Similarly, Sun *et al.* [117] reported that dissociative adsorption is only important during the first few pulses, while direct adsorption becomes more important afterwards. Nevertheless, Hong[29,47] and Pan[42] observed a higher rate of dissociative adsorption throughout the plasma-catalytic process as it becomes more important at higher pressures. Following the discussion in **Dissociative adsorption**, the role of dissociative adsorption is strongly influenced by the reaction conditions and the packing material.

Reactions for production of N and N(s) species are the most energy-intensive steps in ammonia formation. Mehta[44], Iwamoto[10] and van't Veer [34] found that electron impact dissociation of N_2 in plasma is the rate-limiting step. Similar findings were reported by Navascués *et al.*[147] based on their simulations with the surface reaction model. Rouwenhorst [61] argued that since ammonia can be formed under the plasma-only conditions, even a small amount of N radicals can outperform dissociative adsorption of N_2 or vibrationally excited N_2 if a catalyst is present. Furthermore, a direct correlation between the density of N atoms and the ammonia synthesis rate was found, also indicating that dissociation of nitrogen molecules in plasma is the rate-determining step [8,39]. This is in agreement with experimental observations, as higher plasma power enabled a higher NH_3 formation rates to be achieved, since higher plasma power leads to an increase in electron densities, which enhances the rates of reactions involving high energy electrons (including N_2 dissociation) [34,59,62,76,77]. In plasma-only ammonia production, the formation of NH by hydrogenation of N atoms was determined as rate-limiting [39,147]. It should be noted that due to the

complexity of the mechanism, a rate control analysis would be required to definitively determine the rate-limiting step [39,159].

$$N_2 + 2\,surf \rightarrow 2\,N(s) \tag{R22}$$

$$N_2(v) + 2\,surf \rightarrow 2\,N(s) \tag{R23}$$

$$N + surf \rightarrow N(s) \tag{R24}$$

In contrast to H(s), N(s) is recombined to N_2 to a much lesser extent, as it is mostly converted to NH(s) by either E-R (reaction R25) [29,34,37,113,117,140] or L-H mechanism[42,47].

$$N(s) + H \rightarrow NH(s) \tag{R25}$$

$$N(s) + N \rightarrow N_2 + surf \tag{R26}$$

4.4. NH(s)

NH (s) is mainly formed *via* the E-R reactions R15, R17 and R18. Since NH(s) is an important intermediate, this indicates the importance of the E-R reactions in plasma-catalytic ammonia synthesis [29,34,37,113]. Regardless, the results of the mesoscale modeling simulations are not unanimous, which one of these reactions is the predominating formation mechanism of NH(s) production in plasma-catalytic systems. For example, Chen[113] suggested that reactions R15 and R25 are equally important for the formation of ammonia, while Hong[37] reported that the reaction involving N(s) species is strongly favored when the reactor is packed with SiO_2 due to the electronegativity of the N atom. The simulations performed by Sun [117] showed that 92.1 % of NH(s) on Fe/ γ-Al_2O_3 is formed *via* E-R reaction with H(s). Similarly, Andersen *et al.*[39] reported a reaction between ground or electrically excited state N and H(s) over Co/$MgAl_2O_4$ to be dominating in both N_2-rich and H_2-rich feeds. Engelmann *et al.* [8] predicted that both E-R reactions are important on the most noble catalysts, whereas on the less noble metals reactions R15 and R17 are favored. Pan *et al.*[42] even found that 92.6 % of NH(s) were formed via the L-H reaction R18 in their kinetic simulation. Contrary, the reported DFT results suggested that L-H reaction is not possible on SiO_2 surface, as co-adsorption in the adjacent site is not available [37]. It should be noted that the E/N values were different for each simulation, which affects the number density of N and N(s) species[113].

Direct gas-phase NH adsorption has also been considered as another possible route for the production of NH(s) however, its role was mostly minor or even negligible compared to hydrogenation reactions [8,34,37,39,42,47,113,140]. Andersen[39], for example, determined a less than 10 % contribution of direct radical adsorption to overall NH(s) formation.

The main loss mechanisms of NH(s) are further E-R[8,37,113] / L-H [34,39,117,140] hydrogenation to NH_2(s) (reactions R27 and R19) or directly to ammonia[29,34,37,42,47,140] via reaction R28, which gains importance at higher pressures.

$$NH(s) + H \rightarrow NH_2(s) \tag{R27}$$

$$NH(s) + H_2 \rightarrow NH_3 + surf \tag{R28}$$

4.5. NH_2(s)

Similarly to the formation mechanism of NH(s), E-R hydrogenations are considered important in atmospheric-pressure plasma-catalytic systems. The E-R reaction between adsorbed H and the gas-phase NH radical (reaction R(9) was identified as the main formation mechanism of NH_2(s) by Hong[29,37,47] and Pan[42]. Engelmann[8] determined, that the contributions of both E-R reactions (R9 and R27) are significant. Chen *et al.*[113] also found both E-R reactions to be important on alumina, however when reaction between adsorbed NH and gas-phase H (R27) was turned off in the simulation, ammonia molar fraction was 7

orders of magnitude lower compared to when the reaction R(9) was turned off. It should be noted that reaction R28, which is considered to be the main loss mechanism of NH(s), was not included in their model. In 0D plasma kinetic models by van't Veer[34] and Andersen[39], which consider the filamentary nature of DBD discharge, the influence of N_2/H_2 ratio on the importance of L-H hydrogenation of $NH_2(s)$ was demonstrated. In hydrogen-rich conditions the hydrogenation took place through E-R route (reaction R(9) during the microdischarges, while in the duration of the afterglows, when the concentration of gas-phase NH is very low, the L-H hydrogenation (R19) became more significant. In nitrogen-rich conditions the L-H reaction made a more significant contribution to $NH_2(s)$ formation in both regimes[39]. Another possible NH(s) formation is by $NH_2(s)$ direct adsorption of the radical species NH_2 (reaction R29), which does not significantly contribute to the formation of $NH_2(s)$.[113] This was justified by the DFT studies showing that more hydrogenated species NH_x have lower adsorption energies, especially with an increased nitrophilicity of the metal [32].

$$NH_2 + surf \rightarrow NH_2(s) \tag{R29}$$

Hydrogenation of $NH_2(s)$ to ammonia is the dominant surface reaction for ammonia formation and consumption reaction of $NH_2(s)$. L-H hydrogenation (R30) was identified as the main consumption pathway for low-pressure plasma systems[140]. Although the E-R (R31) mechanism becomes more important at atmospheric pressure[37,113,140], hydrogenation has mostly been reported to still mainly occur via the L-H route[8,29,34,39,42,47,117,140], due to the preferential formation of H(s) as a consequence of the lower H_2 dissociation energy compared to N_2.

$$NH_2(s) + H(s) \rightarrow NH_3(s) + surf \tag{R30}$$

$$NH_2(s) + H \rightarrow NH_3 + surf \tag{R31}$$

4.6. NH₃

As already mentioned, ammonia is mainly formed via three-body reactions (R(1) and R(2)) in the initial phase of the synthesis process due to the higher concentration of N_2 and H_2, however surface reactions start to take over when a certain concentration of ammonia is reached [29]. The E-R reaction between NH_2 and H(s) (R16) was determined to be the most important long-term reaction by Hong[29,37,47], while others[8,34,39,113,140] considered L-H hydrogenation (R30) to be dominant. The kinetic model of Van't Veer et al. [34] predicted that reaction R16 is indeed a dominant hydrogenation path in the late afterglows, however, this reaction does not contribute to net ammonia formation, as it is overtaken by dissociation reactions in the microdischarges (R5 and R32). Engelmann et al. [8] found that the L-H reaction becomes more significant between the microcharges, but is still less important than the E-R reaction on the least noble catalysts. Similarly, Liu et al. [32] reported that the L-H reaction can only compete with the E-R hydrogenation reactions over less-nitrophilic metals, such as Sn, Cu, Au, and Ag because the hydrogenation barriers are lower. In addition, the importance of reaction R28, which is typical for thermal ammonia synthesis, has been reported by Hong et al. [29,37], Pan et al. [42] and van't Veer et al. [34]. In kinetic simulations, a spontaneous desorption of ammonia is usually predicted [29,140,141], therefore $NH_3(s)$ species are not considered. Consequently, desorption of ammonia from the surface (reaction R33) was not considered as one of the possible reactions for the generation of NH_3, although this was the case in the model proposed by Sun et al. [133]. Nevertheless, E-R and L-H hydrogenations were determined to be equally important for $NH_3(s)$ formation. To provide a better understanding of the surface reactions, Winter et al. [41] considered not only the adsorbed ammonia but its dissociation by reverse Langmuir-Hinshelwood mechanism (R34) as well. Although, NH and NH_2 radicals are critical gas-phase species at the beginning of the synthesis, when the surface reactions are not yet taking place or their rate is still low, it should be noted that these species are also the

important reactants in ammonia dissociation[29]. The main loss mechanism of ammonia is its dissociation due to collision with high-energy electrons in the gas phase (R5 and R32) [25,29,34,39,147], while in one of their latest works Hong et al. [37] identified the adsorption of NH_3 back onto the surface as an important loss mechanism, but this can be balanced by the facile desorption at sufficient wall temperatures. Ammonia decomposition on the catalyst surface could be another possible loss mechanism of ammonia. However, its influence is negligible even for plasma-activated ammonia, as the reactions between adsorbed species are typically rate-limiting.[38,160] Additional reactions R35 and R36 were introduced as potential source of ammonia consumption when water vapor was used instead of hydrogen in the gas feed mixture[37].

$$NH_3 + e^- \rightarrow e^- + NH_2 + H \tag{R32}$$

$$NH_3(s) \rightarrow NH_3 + surf \tag{R33}$$

$$NH_3(s) + surf \rightarrow NH_2(s) + H(s) \tag{R34}$$

$$NH_3 + O \rightarrow OH + NH_2 \tag{R35}$$

$$NH_3 + OH \rightarrow H_2O + NH_2 \tag{R36}$$

5. Future trends and outlook

Despite of good progress in the development of 0D kinetic models, the complexity of plasma-catalytic ammonia production calls for the higher-dimensional, ideally three-dimensional models with high computational costs [40,95]. As previously reviewed by van't Veer[40], 1D and 2D modeling[161–171] has already been performed, however the modeling was focused on plasma physics rather than the plasma chemistry. Plasma catalysis has been following the development trends in thermal catalysis by using machine learning to study the reaction mechanism and to optimize the synthesis process. A physics-corrected plasma plus deep learning framework DeePlasKin for studying of nonequilibrium discharges has already been developed by Zhu et al. [172]. Pan et al. [42] introduced a multilayer feed-forward deep neural network with a different number of hidden layers and number of neurons per layer to replace the kinetic model and achieve higher accuracy of predicted results. The reduced electric field at time t was used as input, while the ammonia density at time t was the output of the model. To train the neural network, data from kinetic model simulations with different amplitudes of E/N was collected and used as the training set. When the kinetic model was completely replaced by the neural network, a relative error of 4.19×10^{-4} was achieved compared to the numerical results obtained by kinetic model. Furthermore, Zeng et.al[43] developed a multi-parameter model based on Bayesian neural networks (BNNs) to investigate the energy efficient pathways as a function of operational parameters without overfitting. As can be seen in Fig. 6, a probability distribution function was added to each layer of the neural network, allowing the model to also quantify the uncertainties of the predicted results. In this model, voltage, rise time off the power pulse (RT) and gap distance were used as input, while ammonia concentration, energy efficiency (EE) and reactor temperature were the predicted output. It was determined that most of the power is consumed by the gap and the dielectric. The modeling results also shed a light on the influence of the reactor design on the energy efficiency of the process, as the fraction of energy consumed by the current on dielectric depends on the structure of the reactor. By further development of similar models, neural networks could be a powerful tool that could not only be used to study the reaction mechanism, but could also replace a larger number of experiments performed to study the influence of different parameters on ammonia production. It has often been reported that the energy yield of plasma-catalytic ammonia production would be improved by promoting the formation of vibrationally excited nitrogen molecules to fully utilize
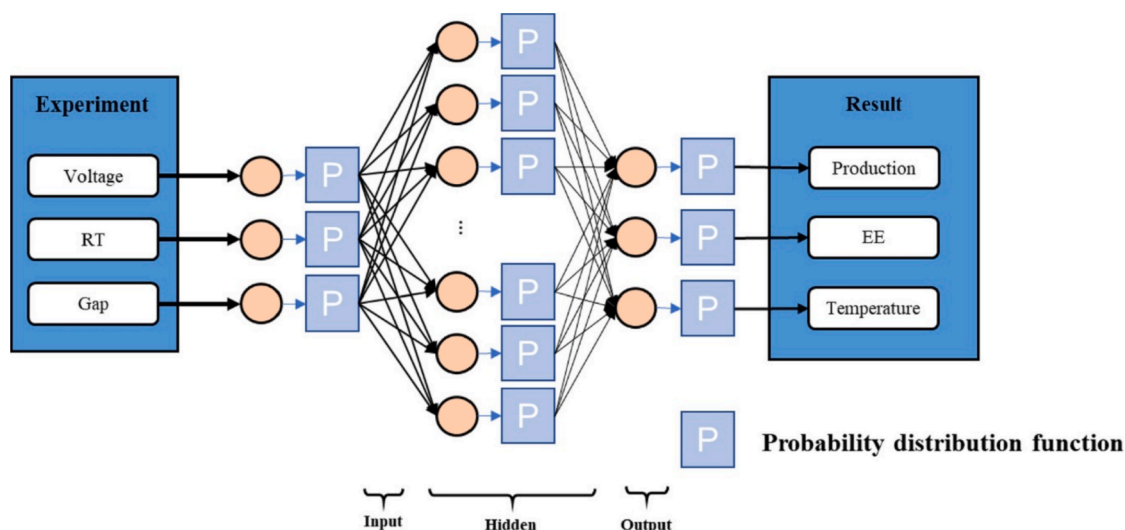
Fig. 6. Structure scheme of BNN multiparameter model. Reproduced with permission from ref [43]. Copyright © 2023 American Chemical Society.

the most efficient catalytic mechanism [21,43,113,173]. In addition to the BNN-based model, a concept of "energy tree" was developed by Li *et al.*[174] to study the energy transfer pathway in collision-dominated plasmas. The "energy tree" describes the energy deposition for the formation of reactive particles (roots), energy transfers between the particles (trunk and branches) and the energy loss due to the interaction with the environment surrounding the plasma, such as electrodes, reactor walls, gasses…(leaves). Although the concept has been successfully applied to some gas mixtures and reaction conditions, further development is needed to achieve higher-dimensional "energy trees" for the description of more complex systems.

As previously discussed, the neural networks are trained using kinetic models which are based on many assumptions, especially with regard to the surface reactions. The rate coefficients are often estimated based on experiments, which are very difficult to fit due to the complexity of the system.[95] The sticking coefficients used in kinetic models are usually estimated to have the same value for all metals [8,113,141]. This could be the case because there are many possible parameters and underlying mechanisms that could have a similar effect on ammonia production, and therefore there appears to be no significant difference in the predicted activities of the metals [83,95]. To definitively determine the values of the sticking coefficients, an *ab initio* molecular dynamics should be applied. Yamijala *et al.*[146] provided the first microscopic description of reactions occurring on active metal sites in low temperature N_2-H_2 plasmas by combining experimental measurements and *ab initio* molecular dynamics computations. The metal type was shown to significantly influence the underlying mechanism, as ammonia was formed through the initial abstraction of H(s) by atomic N on Cu sites, whereas on Pt the surface had to be saturated with NH(s) for ammonia to be produced. Michiels and coworkers[95] proposed the determination of reaction rate coefficients as a function of initial incidence energy and direction, as well as rovibrational state (Eq.42) with the use of sticking coefficients obtained from MD simulations and molecular beam experiments.

$$r = A \bullet \int_{trans} \int_{vib} \int_{rot} \gamma(E_{trans}, \nu, J) \qquad (42)$$

where r is the rate coefficient, A is the impact frequency factor, γ is the sticking coefficient, E_{trans} is the translation energy, ν is the vibrational state and J is the rotational state. However, determining the sticking coefficients with AIMD would be computationally costly, especially for such extensive reaction sets. On the other hand, the numerical values of the rate coefficients for at least each metal surface are necessary to gain

not only a qualitative but also a quantitative insight on plasma-catalytic ammonia production from computational studies. To decrease the computational cost, training of the neural network potentials was presented as a cheaper alternative [49]. Most recently, Cai *et al.*[175] developed a novel hybrid machine learning model, which integrates regression trees, support vector regression and artificial neural networks, to optimize the dry reformation of methane over Ni/Al_2O_3 catalyst in a DBD reactor. To fully implement the use of machine learning for plasma-catalytic systems and the further development of computational models to describe them, it is crucial to improve the accessibility of experimental data in the form of an expanded database with a standardized format for training of models [21,174]. In addition to computational studies, *in-situ* characterization methods are important to gain an understanding of plasma-catalyst interactions, which would contribute to the optimization of plasma-catalytic systems and their implementation on an industrial scale as a Haber-Bosch alternative. Besides *in-situ* Fourier-transform infrared spectroscopy and optical emission spectroscopy used to study plasma-catalytic reactions, *in-situ* scanning electron microscopy has been recently conducted to study micro plasma jets [176–179], which could be further adapted for *in-situ* studies of changes in catalyst surface properties.

Another important future aspect of plasma-catalysis are the supported catalysts. While many of the catalysts consisting of metal particles on non-porous or porous materials have been tested, their full potential has not yet been utilized. The synthesis process plays a crucial role in enhancing the catalytic reactivity, as it significantly influences the distribution, particle size and accessibility of metal nanoparticles. Most of the supported catalysts tested for plasma-catalytic ammonia production have been synthesized using wetness impregnation. Wang *et al.*[26] demonstrated that this method often leads to metal nanoparticles being embedded within the porous framework, particularly in mesoporous supports. Since plasma cannot form inside micro- and mesopores, fewer active metal sites are available for catalytic process. To enhance surface coverage and maximize metal site utilization, Ndayirinde *et al.*[83] increased metal loading to 20 wt% on Al_2O_3-supported catalysts, achieving coverage improvements over the 7–15 % range observed for catalysts with 10 wt% metal. Beside the risk of agglomeration at higher loadings and subsequent decreased activity of the catalyst, increasing the metal loading could have a negative effect on the reaction. As the optimal metals for ammonia production are also used for ammonia decomposition, the later could become the predominant process in the reactor. Additionally, an increase in metal loading leads to pore blockage of the porous supports, which would beat the purpose of using them in the first place, because the diffusion of

ammonia, and consequently its shielding from dissociation in plasma, would be limited. Therefore, it would be beneficial to find a more efficient alternative to wetness impregnation that facilitates metal nanoparticle deposition on the external surface of the support. De Meyer *et al.* [98] reported that Ni/γ-Al$_2$O$_3$ and Co/γ-Al$_2$O$_3$ with the metal loadings of only 1 and 3 wt% prepared by spray-coating outperformed the materials with the same metal loading, prepared *via* wetness impregnation. The improved catalytic activity was attributed to the influence of the material on the plasma discharge regime caused by the difference in the distribution of the metal phase. Catalyst prepared by spray-coating caused plasma discharge to be more homogenous and therefore demoting the ammonia dissociation. Despite the reported limitations of spray coating method, this research clearly demonstrates, that good surface coverage can be achieved at lower metal loadings by implementing a synthesis method, that targets deposition of metal particles on the external surface of the support.

As already established, the motivation for using porous supports comes from their ability to shielding ammonia from dissociation in plasma. As this effect is limited to weak physisorption for SiO$_2$-based support like SBA-15 and MCM-41, Arumuganainar *et al.* [180] studied the influence of incorporation of acid sites by coating of SBA-15 with Al$_2$O$_3$ and incorporation of Al in the MCM-41 framework. While the utilization of acid sides might increase the overall energy yield, it may also require an additional step to recover the adsorbed ammonia by temperature or pressure swing. These finding present an interesting alternative, however further research is required to evaluate the energy efficiency and to determine whether the amount of desorbed ammonia in additional step makes up for the additional energy input it requires. The growing importance of supported catalysts also calls for the more detailed computational studies of metal-support interactions, ammonia diffusion, and related phenomena, which would additionally contribute to the rational catalyst design.

6. Conclusions

A further development in plasma catalysis marks an important step towards the electrification of industrial chemical production. Progress in the optimization of reactor system and catalyst design is limited by the lack of understanding of the underlying mechanisms and synergy between catalyst and plasma. Due to the limitations of experimental studies, such as the lack of *in-situ* characterization techniques, multiscale modeling of the system is crucial to fill the gap in knowledge of plasma-catalytic ammonia production systems. This review summarizes the advances in 0D kinetic modeling and compares the proposed dominant production and consumption pathways of the main reactive species, while also considering atomistic scale modeling. Despite the fact that some of the existing 0D kinetic models implement plasma properties and gas-phase reactions well, especially for the DBD systems, the complexity of the packed-bed systems calls for higher-dimensional models, which would increase both the computational cost and the complexity of the plasma physics and chemistry. To improve the description of surface reactions, additional research in the form of atomistic scale modelling, such as DFT and AIMD, is required. This would allow the determination of numerical values of the reaction rates, yielding quantitative interpretation of the modelling simulations, rather than just qualitative. However, this would be a challenge due to the extensive reaction sets. As the improvement of kinetic models is limited by computational cost, the use of machine learning will be crucial for the further development of the field. To train the machine learning models, an extended database of experimental data is needed. Therefore, combined experimental and computational research is required to reach the full potential of plasma-kinetic ammonia production.

CRediT authorship contribution statement

Katja Vodlan: Writing – review & editing, Writing – original draft,

Conceptualization. **Blaž Likozar:** Supervision, Funding acquisition. **Matej Huš:** Writing – review & editing.

Declaration of competing interest

The authors declare that they have no known competing financial interests or personal relationships that could have appeared to influence the work reported in this paper.

Acknowledgments

Data availability

No data was used for the research described in the article.

References

[1] F. Gorky, A. Best, J. Jasinski, B.J. Allen, A.C. Alba-Rubio, M.L. Carreon, Plasma catalytic ammonia synthesis on Ni nanoparticles: the size effect, J. Catal. 393 (2021) 369–380, https://doi.org/10.1016/j.jcat.2020.11.030.

[2] B.S. Patil, A.S.R. van Kaathoven, F.J.J. Peeters, N. Cherkasov, J. Lang, Q. Wang, V. Hessel, Deciphering the synergy between plasma and catalyst support for ammonia synthesis in a packed dielectric barrier discharge reactor, J. Phys. D Appl. Phys. 53 (2020) 144003, https://doi.org/10.1088/1361-6463/ab6a36.

[3] K.H.R. Rouwenhorst, A.S. Travis, L. Lefferts, 1921–2021: a century of renewable ammonia synthesis, Sustainable Chem. 3 (2022) 149–171, https://doi.org/10.3390/suschem3020011.

[4] C. Fernandez, Chapman Oliver, Brown Marilyn, Hatzell Marta, Achieving Decentralized, Electrified, and Decarbonized Ammonia Production, ChemRxiv (2022).

[5] C. Smith, A.K. Hill, L. Torrente-Murciano, Current and future role of Haber–Bosch ammonia in a carbon-free energy landscape, Energy Environ. Sci. 13 (2020) 331–344, https://doi.org/10.1039/C9EE02873K.

[6] Ž. Ponikvar, B. Likozar, S. Gyergyek, Electrification of catalytic ammonia production and decomposition reactions: from resistance, induction, and dielectric reactor heating to electrolysis, ACS Appl. Energy Mater. 5 (2022) 5457–5472, https://doi.org/10.1021/acsaem.1c03045.

[7] P. Mehta, P. Barboun, D.B. Go, J.C. Hicks, W.F. Schneider, Catalysis enabled by plasma activation of strong chemical bonds: a review, ACS Energy Lett. 4 (2019) 1115–1133, https://doi.org/10.1021/acsenergylett.9b00263.

[8] Y. Engelmann, K. van't Veer, Y. Gorbanev, E.C. Neyts, W.F. Schneider, A. Bogaerts, Plasma catalysis for ammonia synthesis: a microkinetic modeling study on the contributions of Eley–Rideal reactions, ACS Sustain. Chem. Eng. 9 (2021) 13151–13163, https://doi.org/10.1021/acssuschemeng.1c02713.

[9] J.R. Shah, F. Gorky, J. Lucero, M.A. Carreon, M.L. Carreon, Ammonia synthesis via atmospheric plasma catalysis: zeolite 5A, a case of study, Ind. Eng. Chem. Res. 59 (2020) 5167–5176, https://doi.org/10.1021/acs.iecr.9b05220.

[10] M. Iwamoto, M. Akiyama, K. Aihara, T. Deguchi, Ammonia synthesis on wool-like Au, Pt, Pd, Ag, or Cu electrode catalysts in nonthermal atmospheric-pressure plasma of N$_2$ and H$_2$, ACS Catal. 7 (2017) 6924–6929, https://doi.org/10.1021/acscatal.7b01624.

[11] S. Chatterjee, R.K. Parsapur, K.-W. Huang, Limitations of ammonia as a hydrogen energy carrier for the transportation sector, ACS Energy Lett. 6 (2021) 4390–4394, https://doi.org/10.1021/acsenergylett.1c02189.

[12] D. Xie, Y. Sun, T. Zhu, X. Fan, X. Hong, W. Yang, Ammonia synthesis and by-product formation from H$_2$O, H$_2$ and N$_2$ by dielectric barrier discharge combined with an Ru/Al$_2$O$_3$ catalyst, RSC Adv. 6 (2016) 105338–105346, https://doi.org/10.1039/C6RA21351K.

[13] A. Valera-Medina, F. Amer-Hatem, A.K. Azad, I.C. Dedoussi, M. de Joannon, R. X. Fernandes, P. Glarborg, H. Hashemi, X. He, S. Mashruk, J. McGowan, C. Mounaim-Rouselle, A. Ortiz-Prado, A. Ortiz-Valera, I. Rossetti, B. Shu, M. Yehia, H. Xiao, M. Costa, Review on ammonia as a potential fuel: from synthesis to economics, Energy Fuel 35 (2021) 6964–7029, https://doi.org/10.1021/acs.energyfuels.0c03685.

[14] H. Kobayashi, A. Hayakawa, K.D.K.A. Somarathne, E.C. Okafor, Science and technology of ammonia combustion, Proc. Combust. Inst. 37 (2019) 109–133, https://doi.org/10.1016/j.proci.2018.09.029.

[15] D. Zhou, R. Zhou, R. Zhou, B. Liu, T. Zhang, Y. Xian, P.J. Cullen, X. Lu, K. (Ken), Ostrikov, Sustainable ammonia production by non-thermal plasmas: Status, mechanisms, and opportunities, Chem. Eng. J. 421 (2021) 129544, https://doi.org/10.1016/j.cej.2021.129544.

[16] J.G. Chen, R.M. Crooks, L.C. Seefeldt, K.L. Bren, R.M. Bullock, M.Y. Darensbourg, P.L. Holland, B. Hoffman, M.J. Janik, A.K. Jones, M.G. Kanatzidis, P. King, K.M. Lancaster, S. V. Lymar, P. Pfromm, W.F. Schneider, R.R. Schrock, Beyond fossil fuel–driven nitrogen transformations, Science (1979) 360 (2018). https://doi.org/10.1126/science.aar6611.

[17] T. Zhang, R. Zhou, S. Zhang, R. Zhou, J. Ding, F. Li, J. Hong, L. Dou, T. Shao, A. B. Murphy, K. (Ken) Ostrikov, P.J. Cullen, Sustainable ammonia synthesis from nitrogen and water by one-step plasma catalysis, Energy Environ. Mater. 6 (2023), https://doi.org/10.1002/eem2.12344.

[18] J.W. Erisman, M.A. Sutton, J. Galloway, Z. Klimont, W. Winiwarter, How a century of ammonia synthesis changed the world, Nat. Geosci. 1 (2008) 636–639, https://doi.org/10.1038/ngeo325.

[19] F. Gorky, S.R. Guthrie, C.S. Smoljan, J.M. Crawford, M.A. Carreon, M.L. Carreon, Plasma ammonia synthesis over mesoporous silica SBA-15, J. Phys. D Appl. Phys. 54 (2021) 264003, https://doi.org/10.1088/1361-6463/abefbc.

[20] M.L. Carreon, Plasma catalytic ammonia synthesis: state of the art and future directions, J. Phys. D Appl. Phys. 52 (2019) 483001, https://doi.org/10.1088/1361-6463/ab3b2c.

[21] A. Bogaerts, G. Centi, V. Hessel, E. Rebrov, Challenges in unconventional catalysis, Catal. Today 420 (2023) 114180, https://doi.org/10.1016/j.cattod.2023.114180.

[22] L.R. Winter, J.G. Chen, N2 fixation by plasma-activated processes, Joule 5 (2021) 300–315, https://doi.org/10.1016/j.joule.2020.11.009.

[23] P.M. Barboun, H.O. Otor, H. Ma, A. Goswami, W.F. Schneider, J.C. Hicks, Plasma-catalyst reactivity control of surface nitrogen species through plasma-temperature-programmed hydrogenation to ammonia, ACS Sustain. Chem. Eng. 10 (2022) 15741–15748, https://doi.org/10.1021/acssuschemeng.2c04217.

[24] H.-H. Kim, Y. Teramoto, A. Ogata, H. Takagi, T. Nanba, Atmospheric-pressure nonthermal plasma synthesis of ammonia over ruthenium catalysts, Plasma Processes Polym. 14 (2017) 1600157, https://doi.org/10.1002/ppap.201600157.

[25] K.H.R. Rouwenhorst, S. Mani, L. Lefferts, Improving the energy yield of plasma-based ammonia synthesis with in situ adsorption, ACS Sustain. Chem. Eng. 10 (2022) 1994–2000, https://doi.org/10.1021/acssuschemeng.1c08467.

[26] Y. Wang, W. Yang, S. Xu, S. Zhao, G. Chen, A. Weidenkaff, C. Hardacre, X. Fan, J. Huang, X. Tu, Shielding protection by mesoporous catalysts for improving plasma-catalytic ambient ammonia synthesis, J. Am. Chem. Soc. 144 (2022) 12020–12031, https://doi.org/10.1021/jacs.2c01950.

[27] S. Xu, H. Chen, X. Fan, Rational design of catalysts for non-thermal plasma (NTP) catalysis: a reflective review, Catal. Today 419 (2023) 114144, https://doi.org/10.1016/j.cattod.2023.114144.

[28] B. Gordiets, C.M. Ferreira, M.J. Pinheiro, A. Ricard, Self-consistent kinetic model of low-pressure - flowing discharges: II. Surface processes and densities of n, h, species, Plasma Sources Sci Technol 7 (1998) 379–388, https://doi.org/10.1088/0963-0252/7/3/016.

[29] J. Hong, S. Pancheshnyi, E. Tam, J.J. Lowke, S. Prawer, A.B. Murphy, Kinetic modelling of NH 3 production in N 2 –H 2 non-equilibrium atmospheric-pressure plasma catalysis, J. Phys. D Appl. Phys. 50 (2017) 154005, https://doi.org/10.1088/1361-6463/aa6229.

[30] L. Skubic, S. Gyergyek, M. Huš, B. Likozar, A review of multiscale modelling approaches for understanding catalytic ammonia synthesis and decomposition, J. Catal. 429 (2024) 115217, https://doi.org/10.1016/j.jcat.2023.115217.

[31] K. van't Veer, S. van Alphen, A. Remy, Y. Gorbanev, N. De Geyter, R. Snyders, F. Reniers, A. Bogaerts, Spatially and temporally non-uniform plasmas: microdischarges from the perspective of molecules in a packed bed plasma reactor, J. Phys. D Appl. Phys. 54 (2021) 174002, https://doi.org/10.1088/1361-6463/abe15b.

[32] T.-W. Liu, F. Gorky, M.L. Carreon, D.A. Gómez-Gualdrón, Energetics of reaction pathways enabled by N and H radicals during catalytic, plasma-assisted NH 3 synthesis, ACS Sustain. Chem. Eng. 10 (2022) 2034–2051, https://doi.org/10.1021/acssuschemeng.1c05660.

[33] M.J. Banisalman, M.-C. Kim, S.S. Han, Origin of enhanced ammonia synthesis on Ru–Co catalysts unraveled by density functional theory, ACS Catal. 12 (2022) 1090–1097, https://doi.org/10.1021/acscatal.1c05023.

[34] K. van't Veer, Y. Engelmann, F. Reniers, A. Bogaerts, Plasma-catalytic ammonia synthesis in a DBD plasma: role of microdischarges and their afterglows, J. Phys. Chem. C 124 (2020) 22871–22883. https://doi.org/10.1021/acs.jpcc.0c05110.

[35] Z. Chen, S. Jaiswal, A. Diallo, S. Sundaresan, B.E. Koel, Effect of porous catalyst support on plasma-assisted catalysis for ammonia synthesis, Chem. A Eur. J. 126 (2022) 8741–8752, https://doi.org/10.1021/acs.jpca.2c05023.

[36] R. Zhou, D. Zhou, B. Liu, L. Nie, Y. Xian, T. Zhang, R. Zhou, X. Lu, K.K. Ostrikov, P.J. Cullen, Controlling energy transfer in plasma-driven ammonia synthesis by adding helium gas, ACS Sustain. Chem. Eng. 11 (2023) 1828–1836, https://doi.org/10.1021/acssuschemeng.2c06132.

[37] J. Hong, T. Zhang, R. Zhou, L. Dou, S. Zhang, R. Zhou, B. Ashford, T. Shao, A. B. Murphy, K. (Ken) Ostrikov, P.J. Cullen, Green chemical pathway of plasma synthesis of ammonia from nitrogen and water: a comparative kinetic study with a N 2 /H 2 system, Green Chem. 24 (2022) 7458–7468, https://doi.org/10.1039/D2GC02299K.

[38] P. Mehta, P.M. Barboun, Y. Engelmann, D.B. Go, A. Bogaerts, W.F. Schneider, J. C. Hicks, Plasma-Catalytic Ammonia Synthesis beyond the Equilibrium Limit, ACS Catal. 10 (2020) 6726–6734, https://doi.org/10.1021/acscatal.0c00684.

[39] J.A. Andersen, M.C. Holm, K. van't Veer, J.M. Christensen, M. Østberg, A. Bogaerts, A.D. Jensen, Plasma-catalytic ammonia synthesis in a dielectric barrier discharge reactor: a combined experimental study and kinetic modeling, Chem. Eng. J. 457 (2023) 141294, https://doi.org/10.1016/j.cej.2023.141294.

[40] K. van 't Veer, F. Reniers, A. Bogaerts, Zero-dimensional modeling of unpacked and packed bed dielectric barrier discharges: the role of vibrational kinetics in ammonia synthesis, Plasma Sources Sci. Technol. 29 (2020) 045020, https://doi.org/10.1088/1361-6595/ab7a8a.

[41] L.R. Winter, B. Ashford, J. Hong, A.B. Murphy, J.G. Chen, Identifying surface reaction intermediates in plasma catalytic ammonia synthesis, ACS Catal. 10 (2020) 14763–14774, https://doi.org/10.1021/acscatal.0c03166.

[42] J. Pan, Y. Liu, S. Zhang, X. Hu, Y. Liu, T. Shao, Deep learning-assisted pulsed discharge plasma catalysis modeling, Energy Convers. Manag. 277 (2023) 116620, https://doi.org/10.1016/j.enconman.2022.116620.

[43] X. Zeng, S. Zhang, Y. Liu, X. Hu, K.K. Ostrikov, T. Shao, Energy-efficient pathways for pulsed-plasma-activated sustainable ammonia synthesis, ACS Sustain. Chem. Eng. 11 (2023) 1110–1120, https://doi.org/10.1021/acssuschemeng.2c06259.

[44] P. Mehta, P. Barboun, F.A. Herrera, J. Kim, P. Rumbach, D.B. Go, J.C. Hicks, W. F. Schneider, Overcoming ammonia synthesis scaling relations with plasma-enabled catalysis, Nat. Catal. 1 (2018) 269–275, https://doi.org/10.1038/s41929-018-0045-1.

[45] L.D. Pietanza, O. Guaitella, V. Aquilanti, I. Armenise, A. Bogaerts, M. Capitelli, G. Colonna, V. Guerra, R. Engeln, E. Kustova, A. Lombardi, F. Palazzetti, T. Silva, Advances in non-equilibrium $\hbox {CO}_2$ plasma kinetics: a theoretical and experimental review, Eur. Phys. J. D 75 (2021) 237, https://doi.org/10.1140/epjd/s10053-021-00226-0.

[46] N. Van Duc Long, M. Al-Bared, L. Lin, K. Davey, N.N. Tran, N. Pourali, K. Ken Ostrikov, E. Rebrov, V. Hessel, Understanding plasma-assisted ammonia synthesis via crossing discipline borders of literature: a critical review, Chem. Eng. Sci. 263 (2022) 118097, https://doi.org/10.1016/j.ces.2022.118097.

[47] J. Hong, S. Prawer, A.B. Murphy, Plasma catalysis as an alternative route for ammonia production: status, mechanisms, and prospects for progress, ACS Sustain. Chem. Eng. 6 (2018) 15–31, https://doi.org/10.1021/acssuschemeng.7b02381.

[48] E.C. Neyts, K. (Ken) Ostrikov, M.K. Sunkara, A. Bogaerts, Plasma catalysis: synergistic effects at the nanoscale, Chem. Rev. 115 (2015) 13408–13446, https://doi.org/10.1021/acs.chemrev.5b00362.

[49] B. Loenders, R. Michiels, A. Bogaerts, Is a catalyst always beneficial in plasma catalysis? Insights from the many physical and chemical interactions, J. Energy Chem. 85 (2023) 501–533, https://doi.org/10.1016/j.jechem.2023.06.016.

[50] Y. Gorbanev, I. Fedirchyk, A. Bogaerts, Plasma catalysis in ammonia production and decomposition: Use it, or lose it? Curr. Opin. Green Sustain. Chem. 47 (2024) 100916 https://doi.org/10.1016/j.cogsc.2024.100916.

[51] Z. Qu, R. Zhou, J. Sun, Y. Gao, Z. Li, T. Zhang, R. Zhou, D. Liu, X. Tu, P. Cullen, K. (Ken) Ostrikov, Plasma-assisted sustainable nitrogen-to-ammonia fixation: mixed-phase, synergistic processes and mechanisms, ChemSusChem 17 (2024), https://doi.org/10.1002/cssc.202300783.

[52] E.C. Neyts, A. Bogaerts, Understanding plasma catalysis through modelling and simulation—a review, J. Phys. D Appl. Phys. 47 (2014) 224010, https://doi.org/10.1088/0022-3727/47/22/224010.

[53] A. Gómez-Ramírez, J. Cotrino, R.M. Lambert, A.R. González-Elipe, Efficient synthesis of ammonia from N 2 and H 2 alone in a ferroelectric packed-bed DBD reactor, Plasma Sources Sci. Technol. 24 (2015) 065011, https://doi.org/10.1088/0963-0252/24/6/065011.

[54] P. Peng, Y. Li, Y. Cheng, S. Deng, P. Chen, R. Ruan, Atmospheric pressure ammonia synthesis using non-thermal plasma assisted catalysis, Plasma Chem. Plasma Process. 36 (2016) 1201–1210, https://doi.org/10.1007/s11090-016-9713-6.

[55] G. Akay, Sustainable ammonia and advanced symbiotic fertilizer production using catalytic multi-reaction-zone reactors with nonthermal plasma and simultaneous reactive separation, ACS Sustain. Chem. Eng. 5 (2017) 11588–11606, https://doi.org/10.1021/acssuschemeng.7b02962.

[56] P. Peng, Y. Cheng, R. Hatzenbeller, M. Addy, N. Zhou, C. Schiappacasse, D. Chen, Y. Zhang, E. Anderson, Y. Liu, P. Chen, R. Ruan, Ru-based multifunctional mesoporous catalyst for low-pressure and non-thermal plasma synthesis of ammonia, Int. J. Hydrogen Energy 42 (2017) 19056–19066, https://doi.org/10.1016/j.ijhydene.2017.06.118.

[57] G. Akay, K. Zhang, Process intensification in ammonia synthesis using novel coassembled supported microporous catalysts promoted by nonthermal plasma, Ind. Eng. Chem. Res. 56 (2017) 457–468, https://doi.org/10.1021/acs.iecr.6b02053.

[58] Q. Xie, S. Zhuge, X. Song, M. Lu, R. Ruan, Y. Nie, J. Ji, Hydrogenation of plasma-excited nitrogen over an alumina catalyst for ammonia synthesis, Int. J. Hydrogen Energy 43 (2018) 14885–14891, https://doi.org/10.1016/j.ijhydene.2018.06.051.

[59] P. Barboun, P. Mehta, F.A. Herrera, D.B. Go, W.F. Schneider, J.C. Hicks, Distinguishing Plasma contributions to catalyst performance in plasma-assisted ammonia synthesis, ACS Sustain. Chem. Eng. 7 (2019) 8621–8630, https://doi.org/10.1021/acssuschemeng.9b00406.

[60] F.A. Herrera, G.H. Brown, P. Barboun, N. Turan, P. Mehta, W.F. Schneider, J. C. Hicks, D.B. Go, The impact of transition metal catalysts on macroscopic dielectric barrier discharge (DBD) characteristics in an ammonia synthesis plasma catalysis reactor, J. Phys. D Appl. Phys. 52 (2019), https://doi.org/10.1088/1361-6463/ab0c58.

[61] K.H.R. Rouwenhorst, H.-H. Kim, L. Lefferts, Vibrationally excited activation of N 2 in plasma-enhanced catalytic ammonia synthesis: a kinetic analysis, ACS Sustain. Chem. Eng. 7 (2019) 17515–17522, https://doi.org/10.1021/acssuschemeng.9b04997.

[62] Y. Wang, M. Craven, X. Yu, J. Ding, P. Bryant, J. Huang, X. Tu, Plasma-enhanced catalytic synthesis of ammonia over a Ni/Al 2 O 3 catalyst at near-room

temperature: insights into the importance of the catalyst surface on the reaction mechanism, ACS Catal. 9 (2019) 10780–10793, https://doi.org/10.1021/acscatal.9b02538.

[63] P. Peng, P. Chen, M. Addy, Y. Cheng, E. Anderson, N. Zhou, C. Schiappacasse, Y. Zhang, D. Chen, R. Hatzenbeller, Y. Liu, R. Ruan, Atmospheric plasma-assisted ammonia synthesis enhanced via synergistic catalytic absorption, ACS Sustain. Chem. Eng. 7 (2019) 100–104, https://doi.org/10.1021/acssuschemeng.8b03887.

[64] X. Zhu, X. Hu, X. Wu, Y. Cai, H. Zhang, X. Tu, Ammonia synthesis over γ-Al$_2$O$_3$ pellets in a packed-bed dielectric barrier discharge reactor, J. Phys. D Appl. Phys. 53 (2020) 164002, https://doi.org/10.1088/1361-6463/ab6cd1.

[65] S. Li, T. van Raak, F. Gallucci, Investigating the operation parameters for ammonia synthesis in dielectric barrier discharge reactors, J. Phys. D Appl. Phys. 53 (2020) 014008, https://doi.org/10.1088/1361-6463/ab4b37.

[66] X. Hu, X. Zhu, X. Wu, Y. Cai, X. Tu, Plasma-enhanced NH$_3$ synthesis over activated carbon-based catalysts: effect of active metal phase, Plasma Processes Polym. 17 (2020), https://doi.org/10.1002/ppap.202000072.

[67] F. Gorky, M.A. Carreon, M.L. Carreon, Experimental strategies to increase ammonia yield in plasma catalysis over LTA and BEA zeolites, IOP SciNotes 1 (2020) 024801, https://doi.org/10.1088/2633-1357/aba1f8.

[68] Q. Xie, S. Zhuge, X. Song, M. Lu, F. Yu, R. Ruan, Y. Nie, Non-thermal atmospheric plasma synthesis of ammonia in a DBD reactor packed with various catalysts, J. Phys. D Appl. Phys. 53 (2020) 064002, https://doi.org/10.1088/1361-6463/ab57e5.

[69] F. Gorky, J.M. Lucero, J.M. Crawford, B. Blake, M.A. Carreon, M.L. Carreon, Plasma-induced catalytic conversion of nitrogen and hydrogen to ammonia over zeolitic imidazolate frameworks ZIF-8 and ZIF-67, ACS Appl. Mater. Interfaces 13 (2021) 21338–21348, https://doi.org/10.1021/acsami.1c03115.

[70] E. Meloni, L. Cafiero, M. Martino, V. Palma, Structured catalysts for non-thermal plasma-assisted ammonia synthesis, Energies (basel) 16 (2023) 3218, https://doi.org/10.3390/en16073218.

[71] X. Li, Y. Jiao, Y. Cui, C. Dai, P. Ren, C. Song, X. Ma, Synergistic Catalysis of the Synthesis of Ammonia with Co-Based Catalysts and Plasma: From Nanoparticles to a Single Atom, ACS Appl. Mater. Interfaces 13 (2021) 52498–52507, https://doi.org/10.1021/acsami.1c12695.

[72] K.H.R. Rouwenhorst, H.G.B. Burbach, D.W. Vogel, J. Núñez Paulí, B. Geerdink, L. Lefferts, Plasma-catalytic ammonia synthesis beyond thermal equilibrium on Ru-based catalysts in non-thermal plasma, Catal. Sci. Technol. 11 (2021) 2834–2843, https://doi.org/10.1039/D0CY02189J.

[73] M. Iwamoto, M. Horikoshi, R. Hashimoto, K. Shimano, T. Sawaguchi, H. Teduka, M. Matsukata, Higher Activity of Ni/γ-Al2O3 over Fe/γ-Al2O3 and Ru/γ-Al2O3 for Catalytic Ammonia Synthesis in Nonthermal Atmospheric-Pressure Plasma of N2 and H2, Catalysts 10 (2020) 590, https://doi.org/10.3390/catal10050590.

[74] F. Gorky, J.M. Lucero, J.M. Crawford, B. Blake, S.R. Guthrie, M.A. Carreon, M. L. Carreon, Insights on cold plasma ammonia synthesis and decomposition using alkaline earth metal-based perovskites, Catal, Sci. Technol. 11 (2021) 5109–5118, https://doi.org/10.1039/D1CY00729G.

[75] Y. Gorbanev, Y. Engelmann, K. van't Veer, E. Vlasov, C. Ndayirinde, Y. Yi, S. Bals, A. Bogaerts, Al2O3-supported transition metals for plasma-catalytic NH3 synthesis in a DBD plasma: metal activity and insights into mechanisms, Catalysts 11 (2021) 1230, https://doi.org/10.3390/catal11101230.

[76] X. Zhu, J. Liu, X. Hu, Z. Zhou, X. Li, W. Wang, R. Wu, X. Tu, Plasma-catalytic synthesis of ammonia over Ru-based catalysts: Insights into the support effect, J. Energy Inst. 102 (2022) 240–246, https://doi.org/10.1016/j.joei.2022.02.014.

[77] Y. Liu, C.-W. Wang, X.-F. Xu, B.-W. Liu, G.-M. Zhang, Z.-W. Liu, Q. Chen, H.-B. Zhang, Synergistic effect of Co–Ni bimetal on plasma catalytic ammonia synthesis, Plasma Chem. Plasma Process. 42 (2022) 267–282, https://doi.org/10.1007/s11090-021-10223-1.

[78] S. Li, Y. Shao, H. Chen, X. Fan, Nonthermal Plasma catalytic ammonia synthesis over a Ni catalyst supported on MgO/SBA-15, Ind. Eng. Chem. Res. 61 (2022) 3292–3302, https://doi.org/10.1021/acs.iecr.1c04968.

[79] Y. Zhang, S. Li, Z. Yuan, H. Chen, X. Fan, Mechanochemical synthesis of RuCo/MgTiO$_3$ catalysts for nonthermal plasma-assisted ammonia synthesis, Ind. Eng. Chem. Res. 61 (2022) 14199–14210, https://doi.org/10.1021/acs.iecr.2c02216.

[80] H.M. Nguyen, A. Omidkar, W. Li, S. Meng, Z. Li, H. Song, Non-thermal plasma assisted catalytic nitrogen fixation with methane at ambient conditions, Chem. Eng. J. 471 (2023) 144748, https://doi.org/10.1016/j.cej.2023.144748.

[81] J. Feng, P. Ning, K. Li, X. Sun, C. Wang, L. Jia, M. Fan, One-step synthesis of ammonia directly from wet Air/N$_2$ by plasma combined with a γ-Al$_2$O$_3$ Catalyst, ACS Sustain. Chem. Eng. 11 (2023) 804–814, https://doi.org/10.1021/acssuschemeng.2c06706.

[82] H.M. Nguyen, F. Gorky, S. Guthrie, M.L. Carreon, Sustainable ammonia synthesis from nitrogen wet with sea water by single-step plasma catalysis, Catal. Today 418 (2023) 114141, https://doi.org/10.1016/j.cattod.2023.114141.

[83] C. Ndayirinde, Y. Gorbanev, R.-G. Ciocarlan, R. De Meyer, A. Smets, E. Vlasov, S. Bals, P. Cool, A. Bogaerts, Plasma-catalytic ammonia synthesis: Packed catalysts act as plasma modifiers, Catal. Today 419 (2023) 114156, https://doi.org/10.1016/j.cattod.2023.114156.

[84] J. Liu, X. Zhu, S. Jiang, H. Zhang, Y. Hong, G. Chen, X. Tu, Plasma-catalytic synthesis of ammonia over Ru/BaTiO3-based bimetallic catalysts: Synergistic effect from dual-metal active sites, Fuel Process. Technol. 250 (2023) 107851, https://doi.org/10.1016/j.fuproc.2023.107851.

[85] K. Li, S. Chen, H. Wang, F. Wang, Plasma-assisted ammonia synthesis over Ni/LaOF: Dual active centers consisting of oxygen vacancies and Ni, Appl. Catal. A 650 (2023) 118983, https://doi.org/10.1016/j.apcata.2022.118983.

[86] X. Hu, S. Zhang, L. Dou, Y. Gao, C. Zhang, T. Shao, Plasma-enabled sustainable ammonia synthesis at atmospheric pressure: the role of catalysts on synergistic effect, Catal. Today 422 (2023) 114245, https://doi.org/10.1016/j.cattod.2023.114245.

[87] F. Gorky, A. Nambo, M.A. Carreon, M.L. Carreon, Plasma catalytic conversion of nitrogen and hydrogen to ammonia over silico alumino phosphate (SAPO) zeolites, Plasma Chem. Plasma Process. (2023), https://doi.org/10.1007/s11090-023-10397-w.

[88] Y. Liu, X. Xu, Q. Song, Z. Guo, X. Wu, C. Chen, Q. Chen, H. Zhang, Co-Ni/MOF-74 catalyst packed-bed DBD plasma for ammonia synthesis, Plasma Processes Polym. 21 (2024), https://doi.org/10.1002/ppap.202300086.

[89] M. Capone, M. Romanelli, D. Castaldo, G. Parolin, A. Bello, G. Gil, M. Vanzan, A vision for the future of multiscale modeling, ACS Phys. Chem. Au 4 (2024) 202–225, https://doi.org/10.1021/acsphyschemau.3c00080.

[90] L. Skubic, J. Sovdat, N. Teran, M. Huš, D. Kopač, B. Likozar, Ab initio multiscale process modeling of ethane, propane and butane dehydrogenation reactions: a review, Catalysts 10 (2020) 1405, https://doi.org/10.3390/catal10121405.

[91] M. Huš, M. Grilc, A. Pavlišič, B. Likozar, A. Hellman, Multiscale modelling from quantum level to reactor scale: an example of ethylene epoxidation on silver catalysts, Catal. Today 338 (2019) 128–140, https://doi.org/10.1016/j.cattod.2019.05.022.

[92] T. Bligaard, J.K. Nørskov, S. Dahl, J. Matthiesen, C.H. Christensen, J. Sehested, The Brønsted–Evans–Polanyi relation and the volcano curve in heterogeneous catalysis, J. Catal. 224 (2004) 206–217, https://doi.org/10.1016/j.jcat.2004.02.034.

[93] S.A. Akhade, R.M. Nidzyn, G. Rostamikia, M.J. Janik, Using Brønsted-Evans-Polanyi relations to predict electrode potential-dependent activation energies, Catal. Today 312 (2018) 82–91, https://doi.org/10.1016/j.cattod.2018.03.048.

[94] A. Bogaerts, Q.-Z. Zhang, Y.-R. Zhang, K. Van Laer, W. Wang, Burning questions of plasma catalysis: Answers by modeling, Catal. Today 337 (2019) 3–14, https://doi.org/10.1016/j.cattod.2019.04.077.

[95] R. Michiels, N. Gerrits, E. Neyts, A. Bogaerts, Plasma catalysis modeling: how ideal is atomic hydrogen for eley–rideal? J. Phys. Chem. C 128 (2024) 11196–11209, https://doi.org/10.1021/acs.jpcc.4c02193.

[96] S. Chen, Y. Wang, Q. Li, K. Li, M. Li, F. Wang, A DFT study of plasma-catalytic ammonia synthesis: the effect of electric fields, excess electrons and catalyst surfaces on N$_2$ dissociation, PCCP 25 (2023) 3920–3929, https://doi.org/10.1039/D2CP05052H.

[97] K. Shao, A. Mesbah, A study on the role of electric field in low-temperature plasma catalytic ammonia synthesis via integrated density functional theory and microkinetic modeling, JACS Au 4 (2024) 525–544, https://doi.org/10.1021/jacsau.3c00654.

[98] R. De Meyer, Y. Gorbanev, R.-G. Ciocarlan, P. Cool, S. Bals, A. Bogaerts, Importance of plasma discharge characteristics in plasma catalysis: Dry reforming of methane vs. ammonia synthesis, Chem. Eng. J. 488 (2024) 150838, https://doi.org/10.1016/j.cej.2024.150838.

[99] L. Li, J.C. Snyder, I.M. Pelaschier, J. Huang, U. Niranjan, P. Duncan, M. Rupp, K. Müller, K. Burke, Understanding machine-learned density functionals, Int. J. Quantum Chem 116 (2016) 819–833, https://doi.org/10.1002/qua.25040.

[100] H. Zhu, Z. Guo, D. Lan, S. Liu, M. Liu, J. Zhang, X. Luo, J. Yu, T. Wu, Accelerating the design of catalysts for CO2 electroreduction to HCOOH: A data-driven DFT-ML screening of dual atom catalysts, J. Energy Chem. 99 (2024) 627–635, https://doi.org/10.1016/j.jechem.2024.08.015.

[101] M. Rittiruam, P. Khamloet, S. Tiwtusthada, A. Ektarawong, T. Saelee, C. Atthapak, P. Khajondetchairit, B. Alling, P. Prasertham, S. Praserthdam, Machine-learning-accelerated density functional theory screening of Cu-based high-entropy alloys for carbon dioxide reduction to ethylene, Appl. Surf. Sci. 684 (2025) 161919, https://doi.org/10.1016/j.apsusc.2024.161919.

[102] M. Tamtaji, M. Kazemeini, J. Abdi, DFT and machine learning studies on a multi-functional single-atom catalyst for enhanced oxygen and hydrogen evolution as well as CO2 reduction reactions, Int. J. Hydrogen Energy 80 (2024) 1075–1083, https://doi.org/10.1016/j.ijhydene.2024.07.244.

[103] Y. Guan, T. Lee, K. Wang, S. Yu, J.C. McWilliams, S$_N$Ar regioselectivity predictions: machine learning triggering DFT reaction modeling through statistical threshold, J. Chem. Inf. Model. 63 (2023) 3751–3760, https://doi.org/10.1021/acs.jcim.3c00580.

[104] G. Piccini, M.-S. Lee, S.F. Yuk, D. Zhang, G. Collinge, L. Kollias, M.-T. Nguyen, V.-A. Glezakou, R. Rousseau, *Ab initio* molecular dynamics with enhanced sampling in heterogeneous catalysis, Catal. Sci. Technol. 12 (2022) 12–37, https://doi.org/10.1039/D1CY01329G.

[105] X. Lu, Q. Chen, N. Liu, J. Chen, M. Zhang, J. Sun, Plasma-catalytic assisted ammonia synthesis: Reactive molecular dynamics study, J. Energy Inst. 118 (2025) 101919, https://doi.org/10.1016/j.joei.2024.101919.

[106] Z. Chen, Z. Liu, X. Xu, XPK: toward accurate and efficient microkinetic modeling in heterogeneous catalysis, ACS Catal. 13 (2023) 15219–15229, https://doi.org/10.1021/acscatal.3c04298.

[107] D.G. Vlachos, A.B. Mhadeshwar, N.S. Kaisare, Hierarchical multiscale model-based design of experiments, catalysts, and reactors for fuel processing, Comput. Chem. Eng. 30 (2006) 1712–1724, https://doi.org/10.1016/j.compchemeng.2006.05.033.

[108] K. Van Laer, A. Bogaerts, Fluid modelling of a packed bed dielectric barrier discharge plasma reactor, Plasma Sources Sci. Technol. 25 (2016) 015002, https://doi.org/10.1088/0963-0252/25/1/015002.

[109] Y.-R. Zhang, K. Van Laer, E.C. Neyts, A. Bogaerts, Can plasma be formed in catalyst pores? a modeling investigation, Appl. Catal. B 185 (2016) 56–67, https://doi.org/10.1016/j.apcatb.2015.12.009.

[110] Y.-R. Zhang, E.C. Neyts, A. Bogaerts, Influence of the material dielectric constant on plasma generation inside catalyst pores, J. Phys. Chem. C 120 (2016) 25923–25934, https://doi.org/10.1021/acs.jpcc.6b09038.

[111] Y.-R. Zhang, E.C. Neyts, A. Bogaerts, Enhancement of plasma generation in catalyst pores with different shapes, Plasma Sources Sci. Technol. 27 (2018) 055008, https://doi.org/10.1088/1361-6595/aac0e4.

[112] S. Pancheshnyi, B. Eismann, G.J.M. Hagelaar, L.C. Pitchford, Computer code ZDPlasKin, (2008).

[113] Z. Chen, B.E. Koel, S. Sundaresan, Plasma-assisted catalysis for ammonia synthesis in a dielectric barrier discharge reactor: key surface reaction steps and potential causes of low energy yield, J. Phys. D Appl. Phys. 55 (2022) 055202, https://doi.org/10.1088/1361-6463/ac2f12.

[114] G.J.M. Hagelaar, L.C. Pitchford, Solving the Boltzmann equation to obtain electron transport coefficients and rate coefficients for fluid models, Plasma Sources Sci. Technol. 14 (2005) 722–733, https://doi.org/10.1088/0963-0252/14/4/011.

[115] R. Brandenburg, Dielectric barrier discharges: progress on plasma sources and on the understanding of regimes and single filaments, Plasma Sources Sci. Technol. 26 (2017) 053001, https://doi.org/10.1088/1361-6595/aa6426.

[116] Z.-I. Mujahid, I. Korolov, Y. Liu, T. Mussenbrock, J. Schulze, Propagation dynamics and interaction of multiple streamers at and above adjacent dielectric pellets in a packed bed plasma reactor, J. Phys. D Appl. Phys. 55 (2022) 495201, https://doi.org/10.1088/1361-6463/ac99ea.

[117] J. Sun, Q. Chen, X. Zhao, H. Lin, W. Qin, Kinetic investigation of plasma catalytic synthesis of ammonia: insights into the role of excited states and plasma-enhanced surface chemistry, Plasma Sources Sci. Technol. 31 (2022) 094009, https://doi.org/10.1088/1361-6595/ac8e2c.

[118] J.A. Andersen, K. van 't Veer, J.M. Christensen, M. Østberg, A. Bogaerts, A.D. Jensen, Ammonia decomposition in a dielectric barrier discharge plasma: Insights from experiments and kinetic modeling, Chem Eng Sci 271 (2023) 118550. https://doi.org/10.1016/j.ces.2023.118550.

[119] J.A. Andersen, J.M. Christensen, M. Østberg, A. Bogaerts, A.D. Jensen, Plasma-catalytic ammonia decomposition using a packed-bed dielectric barrier discharge reactor, Int. J. Hydrogen Energy 47 (2022) 32081–32091, https://doi.org/10.1016/j.ijhydene.2022.07.102.

[120] N. Liu, X. Mao, C. Kondratowicz, T.Y. Chen, B. Mei, Z. Wang, Y. Xu, H. Zhong, Z. Shi, A. Morozov, A. Dogariu, Y. Ju, Unraveling nonequilibrium generation of atomic nitrogen and hydrogen in plasma-aided ammonia synthesis, ACS Energy Lett. 9 (2024) 2031–2036, https://doi.org/10.1021/acsenergylett.4c00729.

[121] F.J.J. Peeters, M.C.M. van de Sanden, The influence of partial surface discharging on the electrical characterization of DBDs, Plasma Sources Sci. Technol. 24 (2014) 015016, https://doi.org/10.1088/0963-0252/24/1/015016.

[122] K.W. Engeling, J. Kruszelnicki, M.J. Kushner, J.E. Foster, Time-resolved evolution of micro-discharges, surface ionization waves and plasma propagation in a two-dimensional packed bed reactor, Plasma Sources Sci. Technol. 27 (2018) 085002, https://doi.org/10.1088/1361-6595/aad2c5.

[123] W. Wang, H.-H. Kim, K. Van Laer, A. Bogaerts, Streamer propagation in a packed bed reactor for plasma catalysis applications, Chem. Eng. J. 334 (2018) 2467–2479, https://doi.org/10.1016/j.cej.2017.11.139.

[124] H. Zhu, P. Zhang, S. Dai, Recent advances of lanthanum-based perovskite oxides for catalysis, ACS Catal. 5 (2015) 6370–6385, https://doi.org/10.1021/acscatal.5b01667.

[125] J. Liu, X. Zhu, X. Hu, X. Tu, Plasma-assisted ammonia synthesis in a packed-bed dielectric barrier discharge reactor: roles of dielectric constant and thermal conductivity of packing materials, Plasma Sci. Technol 24 (2022) 025503, https://doi.org/10.1088/2058-6272/ac39fb.

[126] H. Fang, D. Liu, Y. Luo, Y. Zhou, S. Liang, X. Wang, B. Lin, L. Jiang, Challenges and opportunities of Ru-based catalysts toward the synthesis and utilization of ammonia, ACS Catal. 12 (2022) 3938–3954, https://doi.org/10.1021/acscatal.2c00090.

[127] H.-H. Kim, J.-H. Kim, A. Ogata, Microscopic observation of discharge plasma on the surface of zeolites supported metal nanoparticles, J. Phys. D Appl. Phys. 42 (2009) 135210, https://doi.org/10.1088/0022-3727/42/13/135210.

[128] B.S. Patil, N. Cherkasov, N.V. Srinath, J. Lang, A.O. Ibhadon, Q. Wang, V. Hessel, The role of heterogeneous catalysts in the plasma-catalytic ammonia synthesis, Catal. Today 362 (2021) 2–10, https://doi.org/10.1016/j.cattod.2020.06.074.

[129] T.A.B.J. van Raak, S. Li, F. Gallucci, Prevailing surface reactions in the plasma-catalytic ammonia synthesis with Ru/CeO2 and Ru/Ti-CeO2, Chem. Eng. J. 455 (2023) 140691, https://doi.org/10.1016/j.cej.2022.140691.

[130] Y. Wu, C. Li, B. Fang, X. Wang, J. Ni, B. Lin, J. Lin, L. Jiang, Enhanced ammonia synthesis performance of ceria-supported Ru catalysts *via* introduction of titanium, Chem. Commun. 56 (2020) 1141–1144, https://doi.org/10.1039/C9CC07385J.

[131] J. Shah, T. Wu, J. Lucero, M.A. Carreon, M.L. Carreon, Nonthermal plasma synthesis of ammonia over Ni-MOF-74, ACS Sustain. Chem. Eng. 7 (2019) 377–383, https://doi.org/10.1021/acssuschemeng.8b03705.

[132] K.S. Yin, M. Venugopalan, Plasma chemical synthesis. I. Effect of electrode material on the synthesis of ammonia, Plasma Chem. Plasma Process. 3 (1983) 343–350, https://doi.org/10.1007/BF00564632.

[133] J. Sun, Q. Chen, X. Yang, B.E. Koel, Effects of non-equilibrium excitation on methane oxidation in a low-temperature RF discharge, J. Phys. D Appl. Phys. 53 (2020) 064001, https://doi.org/10.1088/1361-6463/ab57dc.

[134] J. Sun, Q. Chen, Kinetic roles of vibrational excitation in RF plasma assisted methane pyrolysis, J. Energy Chem. 39 (2019) 188–197, https://doi.org/10.1016/j.jechem.2019.01.028.

[135] Q. Chen, X. Yang, J. Sun, X. Zhang, X. Mao, Y. Ju, B.E. Koel, Pyrolysis and oxidation of methane in a RF plasma reactor, Plasma Process. 37 (2017) 1551–1571, https://doi.org/10.1007/s11090-017-9844-4.

[136] V. Kotov, Two-modes approach to the state-to-state vibrational kinetics of CO 2, J. Phys. B Atomic Mol. Phys. 53 (2020) 175104, https://doi.org/10.1088/1361-6455/ab9d01.

[137] Y.M. Kedalo, A.A. Knizhnik, B.V. Potapkin, Applicability of the fridman–macheret α-model to heterogeneous processes in the case of dissociative adsorption of N 2 on the Ru surface, J. Phys. Chem. C 127 (2023) 11536–11541, https://doi.org/10.1021/acs.jpcc.3c01967.

[138] A. Fridman, Plasma Chemistry, Cambridge University Press, 2008, 10.1017/CBO9780511546075.

[139] K.H.R. Rouwenhorstm, L. Lefferts, Plasma-catalytic ammonia synthesis via eley-rideal reactions: a kinetic analysis, ChemCatChem 15 (2023), https://doi.org/10.1002/cctc.202300078.

[140] J. Shah, W. Wang, A. Bogaerts, M.L. Carreon, Ammonia synthesis by radio frequency plasma catalysis: revealing the underlying mechanisms, ACS Appl. Energy Mater. 1 (2018) 4824–4839, https://doi.org/10.1021/acsaem.8b00898.

[141] E. Carrasco, M. Jiménez-Redondo, I. Tanarro, V.J. Herrero, Neutral and ion chemistry in low pressure dc plasmas of H2/N2 mixtures: routes for the efficient production of NH3 and NH4+, PCCP 13 (2011) 19561, https://doi.org/10.1039/c1cp22284h.

[142] P.J. Chantry, A simple formula for diffusion calculations involving wall reflection and low density, J. Appl. Phys. 62 (1987) 1141–1148, https://doi.org/10.1063/1.339662.

[143] B. Gordiets, C.M. Ferreira, M.J. Pinheiro, A. Ricard, Self-consistent kinetic model of low-pressure - flowing discharges: I. Volume processes, Plasma Sources Sci Technol 7 (1998) 363–378, https://doi.org/10.1088/0963-0252/7/3/015.

[144] E.N. Fuller, P.D. Schettler, J.C. Giddings, A new method for prediction of binary gas-phase diffusion coefficients, Ind. Eng. Chem. 58 (1966) 19–27.

[145] R.D. Cortright, J.A. Dumesic, Kinetics of heterogeneous catalytic reactions: Analysis of reaction schemes, in: 2001: pp. 161–264. https://doi.org/10.1016/S0360-0564(02)46023-3.

[146] S.S.R.K.C. Yamijala, G. Nava, Z.A. Ali, D. Beretta, B.M. Wong, L. Mangolini, Harnessing plasma environments for ammonia catalysis: mechanistic insights from experiments and large-scale *Ab Initio* molecular dynamics, J. Phys. Chem. Lett. 11 (2020) 10469–10475, https://doi.org/10.1021/acs.jpclett.0c03021.

[147] P. Navascués, J.M. Obrero-Pérez, J. Cotrino, A.R. González-Elipe, A. Gómez-Ramírez, Unraveling discharge and surface mechanisms in plasma-assisted ammonia reactions, ACS Sustain. Chem. Eng. 8 (2020) 14855–14866, https://doi.org/10.1021/acssuschemeng.0c04461.

[148] H. Zhao, G. Song, Z. Chen, X. Yang, C. Yan, S. Abe, Y. Ju, S. Sundaresan, B.E. Koel, *In Situ* Identification of NNH and N 2 H 2 by using molecular-beam mass spectrometry in plasma-assisted catalysis for NH 3 synthesis, ACS Energy Lett. 7 (2022) 53–58, https://doi.org/10.1021/acsenergylett.1c02207.

[149] J. Shah, F. Gorky, P. Psarras, B. Seong, D.A. Gómez-Gualdrón, M.L. Carreon, Enhancement of the yield of ammonia by hydrogen-sink effect during plasma catalysis, ChemCatChem 12 (2020) 1200–1211, https://doi.org/10.1002/cctc.201901769.

[150] M. Sajid, W.E. Kaden, A. Kara, DFT investigation of ammonia formation via a langmuir–hinshelwood mechanism on Mo-terminated δ-MoN(0001), ACS Omega 7 (2022) 4277–4285, https://doi.org/10.1021/acsomega.1c05967.

[151] J. Qian, Q. An, A. Fortunelli, R.J. Nielsen, W.A. Goddard, Reaction mechanism and kinetics for ammonia synthesis on the Fe(111) Surface, J. Am. Chem. Soc. 140 (2018) 6288–6297, https://doi.org/10.1021/jacs.7b13409.

[152] C. Kim, J. Lee, S. Lee, A new ammonia kinetic model in ru-catalyzed steam-reforming reaction containing N2 in natural gas, Catalysts 13 (2023) 1380, https://doi.org/10.3390/catal13101380.

[153] M. El-Shafie, A comprehensive assessment of ammonia synthesis reaction kinetics and rate equations, Int. J. Hydrogen Energy 48 (2023) 35938–35952, https://doi.org/10.1016/j.ijhydene.2023.06.011.

[154] O. Galparsoro, J.I. Juaristi, C. Crespos, M. Alducin, P. Larrégaray, Stereodynamics of Diatom Formation through Eley–Rideal Abstraction, J. Phys. Chem. C 121 (2017) 19849–19858, https://doi.org/10.1021/acs.jpcc.7b06529.

[155] T. Mizushima, K. Matsumoto, H. Ohkita, N. Kakuta, Catalytic effects of metal-loaded membrane-like alumina tubes on ammonia synthesis in atmospheric pressure plasma by dielectric barrier discharge, Plasma Chem. Plasma Process. 27 (2007) 1–11, https://doi.org/10.1007/s11090-006-9034-2.

[156] G.D. Billing, A. Guldberg, N.E. Henriksen, F.Y. Hansen, Dissociative chemisorption of N2 on rhenium: dynamics at low impact energies, Chem. Phys. 147 (1990) 1–11, https://doi.org/10.1016/0301-0104(90)85015-O.

[157] F.Y. Hansen, N.E. Henriksen, G.D. Billing, A. Guldberg, Catalytic synthesis of ammonia using vibrationally excited nitrogen molecules: theoretical calculation of equilibrium and rate constants, Surf. Sci. 264 (1992) 225–234, https://doi.org/10.1016/0039-6028(92)90180-E.

[158] C.T. Rettner, H. Stein, Effect of vibrational energy on the dissociative chemisorption of N2 on Fe(111), J. Chem. Phys. 87 (1987) 770–771, https://doi.org/10.1063/1.453575.

[159] C. Stegelmann, A. Andreasen, C.T. Campbell, Degree of rate control: how much the energies of intermediates and transition states control rates, J. Am. Chem. Soc. 131 (2009) 8077–8082, https://doi.org/10.1021/ja9000097.

[160] D.A. Hansgen, D.G. Vlachos, J.G. Chen, Using first principles to predict bimetallic catalysts for the ammonia decomposition reaction, Nat. Chem. 2 (2010) 484–489, https://doi.org/10.1038/nchem.626.

[161] K. Kourtzanidis, Full cycle, self-consistent, two-dimensional analysis of a packed bed DBD reactor for plasma-assisted CO2 splitting: spatiotemporal

inhomogeneous, glow to streamer to surface discharge transitions, Plasma Sources Sci. Technol. 32 (2023) 105016, https://doi.org/10.1088/1361-6595/ad0430.

[162] S. Bayki, S. Mujumdar, A 1D model for prediction of dry electrical discharge machining (dry-EDM) plasma characteristics, J. Manuf. Process. 102 (2023) 417–428, https://doi.org/10.1016/j.jmapro.2023.07.036.

[163] K. Takaki, J.-S. Chang, K.G. Kostov, Atmospheric pressure of nitrogen plasmas in a ferro-electric packed bed barrier discharge reactor part I: modeling, IEEE Trans. Dielectr. Electr. Insul. 11 (2004) 281–290, https://doi.org/10.1109/TDEI.2004.1306726.

[164] K.G. Jen-Shih Chang, K. Kostov, T. Urashima, Y. Yamamoto, T. Okayasu, T. Kato, K.Y. Iwaizumi, Removal of NF/sub 3/ from semiconductor-process flue gases by tandem packed-bed plasma and adsorbent hybrid systems, IEEE Trans. Ind. Appl. 36 (2000) 1251–1259, https://doi.org/10.1109/28.871272.

[165] H. Russ, M. Neiger, J.E. Lang, Simulation of micro discharges for the optimization of energy requirements for removal of NO/sub x/ from exhaust gases, IEEE Trans. Plasma Sci. 27 (1999) 38–39, https://doi.org/10.1109/27.763019.

[166] A.A. Kulikovsky, Positive streamer between parallel plate electrodes in atmospheric pressure air, J. Phys. D Appl. Phys. 30 (1997) 441–450, https://doi.org/10.1088/0022-3727/30/3/017.

[167] Woo Seok Kang, Jin Myung Park, Yongho Kim, Sang Hee Hong, Numerical study on influences of barrier arrangements on dielectric barrier discharge characteristics, IEEE Transactions on Plasma Science 31 (2003) 504–510. https://doi.org/10.1109/TPS.2003.815469.

[168] J. Kruszelnicki, K.W. Engeling, J.E. Foster, Z. Xiong, M.J. Kushner, Propagation of negative electrical discharges through 2-dimensional packed bed reactors, J. Phys. D Appl. Phys. 50 (2017) 025203, https://doi.org/10.1088/1361-6463/50/2/025203.

[169] R. Dorai, M.J. Kushner, A model for plasma modification of polypropylene using atmospheric pressure discharges, J. Phys. D Appl. Phys. 36 (2003) 666–685, https://doi.org/10.1088/0022-3727/36/6/309.

[170] N.Y. Babaeva, A.N. Bhoj, M.J. Kushner, Streamer dynamics in gases containing dust particles, Plasma Sources Sci. Technol. 15 (2006) 591–602, https://doi.org/10.1088/0963-0252/15/4/001.

[171] N.Y. Babaeva, M.J. Kushner, Effect of inhomogeneities on streamer propagation: II. Streamer Dynamics in High Pressure Humid Air with Bubbles, Plasma Sources Sci. Technol. 18 (2009) 035010, https://doi.org/10.1088/0963-0252/18/3/035010.

[172] Y. Zhu, Y. Bo, X. Chen, Y. Wu, Tailoring electric field signals of nonequilibrium discharges by the deep learning method and physical corrections, Plasma Processes Polym. 19 (2022), https://doi.org/10.1002/ppap.202100155.

[173] K.H.R. Rouwenhorst, Y. Engelmann, K. van 't Veer, R.S. Postma, A. Bogaerts, L. Lefferts, Plasma-driven catalysis: green ammonia synthesis with intermittent electricity, Green Chem. 22 (2020) 6258–6287, https://doi.org/10.1039/D0GC02058C.

[174] H.-P. Li, K. (Ken) Ostrikov, W. Sun, The energy tree: Non-equilibrium energy transfer in collision-dominated plasmas, Phys. Rep. 770–772 (2018) 1–45, https://doi.org/10.1016/j.physrep.2018.08.002.

[175] Y. Cai, D. Mei, Y. Chen, A. Bogaerts, X. Tu, Machine learning-driven optimization of plasma-catalytic dry reforming of methane, J. Energy Chem. 96 (2024) 153–163, https://doi.org/10.1016/j.jechem.2024.04.022.

[176] L. Grünewald, D. Chezganov, R. De Meyer, A. Orekhov, S. Van Aert, A. Bogaerts, S. Bals, J. Verbeeck, In situ plasma studies using a direct current microplasma in a scanning electron microscope, Adv. Mater. Technol. (2024), https://doi.org/10.1002/admt.202301632.

[177] K. Matra, Y. Mizobuchi, H. Furuta, A. Hatta, Local sputter etching by micro plasma jet in SEM, Vacuum 87 (2013) 132–135, https://doi.org/10.1016/j.vacuum.2012.03.011.

[178] K. Tomatsu, K. Kobayashi, T. Suzuki, T. Aoki, T. Omura, A. Hatta, <i>In-Situ</i> Scanning Electron Microscope Observation of Hydrogen Embrittlement in High-Strength Low-Alloy Steel by Near Atmospheric-Pressure Hydrogen Microplasma Jet, SSRN Electronic Journal (2022). https://doi.org/10.2139/ssrn.4180429.

[179] K. Tomatsu, T. Aoki, K. Kobayashi, T. Omura, A. Hatta, *In situ* scanning electron microscopy of hydrogen embrittlement by near atmospheric-pressure hydrogen microplasma jet, Rev. Sci. Instrum. 94 (2023), https://doi.org/10.1063/5.0129618.

[180] S.E. Arumuganainar, S. Sartzetakis, C.W. Hullfish, B.E. Koel, M.L. Sarazen, Influence of ordered mesoporous oxides in plasma-assisted ammonia synthesis, Energy Fuel 38 (2024) 23150–23166, https://doi.org/10.1021/acs.energyfuels.4c03270.